Global Characteristics of Ocean Variability Estimated from Regional TOPEX/POSEIDON Altimeter Measurements

DETLEF STAMMER

Department of Earth, Atmospheric and Planetary Sciences, Massachusetts Institute of Technology, Cambridge, Massachusetts

(Manuscript received 7 May 1996, in final form 10 February 1997)

ABSTRACT

Three years of altimetric data from the TOPEX/POSEIDON spacecraft have been used to study characteristics of eddy variability over the World Ocean. The nature of the variability and its spatial structure are characterized in terms of the geographical distribution of eddy energy, as simple approximations of observed regional frequency and wavenumber spectra, and in terms of associated eddy time and space scales of sea surface height (SSH) variability and geostrophic velocity. Emphasis is put on summarizing characteristics typical for dynamically distinct regions of the World Ocean. This effort results in an attempt to describe the observed ocean variability in terms of universal spectral relations that depend only on few mean flow parameters such as the first-mode Rossby radius of deformation. Regional peculiarities follow naturally as deviations from the fundamental frequency and wavenumber spectra presented here.

Frequency spectra of both variables can be summarized by three basic types representing (i) the energetic boundary currents, (ii) the bulk of the extratropical basins, and (iii) the tropical interior oceans. Extratropical wavenumber spectra suggest a geostrophically turbulent ocean. They are basically uniform in shape and show a plateau on long wavelength for SSH and a steep spectral decay close to k^{-5} toward smaller wavelengths. The transition between both regimes shifts toward longer cutoff wavenumbers from low to high latitudes, and related spatial eddy scales can be described in terms of the first-mode Rossby deformation radius of the mean flow field. Although consistent with estimated Rhines scales in low latitudes, inferred eddy scales are up to a factor of 0.3 smaller at high latitudes.

1. Introduction

Ocean variability is broadband and, in general, dominated by mesoscale fluctuations on timescales between 20 and 150 days and spatial scales between 50 and 500 km (Wyrtki et al. 1976; Danzler 1977; Richman et al. 1977). Because eddies transport heat and momentum and interact with the mean flow field, it is important to understand eddy dynamics, their transport properties, and their impact on climate.

A detailed understanding of eddy dynamics and related eddy mixing in the World Ocean is missing, partly because of the previous lack of adequate ocean observations. Earlier field experiments during the mid-1970s suggested that eddy energy is generated primarily by instability processes of intense boundary currents (MODE Group 1978; McWilliams et al. 1983; Robinson 1983) and is radiated subsequently into the interior ocean by Rossby waves (Pedlosky 1977; Talley 1983; Hogg 1988). Direct atmospheric forcing by variable wind stress (Müller and Frankignoul 1981) was considered to be another important eddy source term in areas remote from intense currents. In addition, small-scale topography can transfer large-scale (barotropic) energy, enhanced by surface wind forcing or Helmholz-type shear instability, to smaller baroclinic scales through mode–mode coupling (Trèguier and Hua 1988). The geographical variation of eddy amplitude and eddy scales (Mercier and Colin de Verdière 1985; Krauss et al. 1990; Stammer and Böning 1992) presents a particularly formidable challenge to the understanding of ocean eddy dynamics and eddy source terms, and requires a systematic regional investigation of observed eddy characteristics. Comprehensive reviews on oceanic variability based on in situ time series of moored current meter and thermistor records were published by Wunsch (1981) and Schmitz and Luyten (1991).

In the last century, enhanced insight was gained into the generation and distribution of the oceanic mesoscale through the application of modern measurement technologies or the advanced developments in numerical ocean simulations. Stammer and Böning (1996, SB96 henceforth) give a recent review on that subject, in which they refer to satellite altimetry as a vital observational element in gaining further insight into oceanic low-frequency variability through its unique sampling characteristics.

Corresponding author address: Dr. Detlef Stammer, Dept. of Earth, Atmospheric, and Planetary Sciences, Massachusetts Institute of Technology, Room 54-1518, Cambridge, MA 02139-4307.
E-mail: detlef@lagoon.mit.edu

A full discussion of near-surface variability involves an analysis of underlying dynamical principles, and this attempt is intimately connected to the compilation of frequency–wavenumber spectra. From two years of high quality TOPEX/POSEIDON (T/P) data, Wunsch and Stammer (1995, henceforth WS95) constructed the first global frequency–wavenumber spectrum of sea surface height (SSH) variability and associated one-dimensional frequency and wavenumber spectra for SSH and sea surface slope. These spectra are important references against which to measure local variations. For a comprehensive dynamical interpretation, however, a detailed regional study is required.

In this paper, based on three years of high quality altimeter observations now available from the T/P mission, various aspects of regional eddy characteristics are analyzed over the World Ocean. Our main objective is to summarize characteristics common to dynamically similar parts of the ocean, thereby simplifying the otherwise overwhelming amount of detail inherent in the T/P observations. Results will be used as the basis for a dynamical interpretation of the observed eddy field, an effort which naturally leads to a discussion of universal aspects of ocean variability. Regional details will emerge subsequently as deviations from the references given here. Although some of the provided estimates are readily available from previous Geosat data (e.g., Fu 1983; Fu and Zlotnicki 1989; Wunsch 1991; Le Traon et al. 1990; Le Traon 1991; Stammer and Böning 1992), their intrinsic uncertainties made previous dynamical interpretation speculative and controversial (see Le Traon 1993 and Stammer and Böning 1993).

The geographical distribution of eddy characteristics and their relation to mean flow properties can shed important light onto questions regarding eddy generation mechanisms and eddy–mean flow interactions. Here we will demonstrate a correlation of the observed geographical distribution of eddy variability with mean flow horizontal density gradients (which are related to the mean available potential energy) and discuss a relation of eddy length scales inferred from T/P data, with a first-mode Rossby radius of deformation and a Rhines scale, both of dynamical significance. In a second part of this study (Stammer; 1997), present results on eddy statistics are interpreted in the context of the theory of a baroclinically unstable flow field as pioneered by Green (1970) and Stone (1972) for atmospheric conditions. T/P eddy statistics will also be used there to provide an estimate of a horizontally varying field of eddy diffusivity, as well as resulting eddy heat and salt transports.

TOPEX/POSEIDON data from the period 1 December 1992 through 27 November 1995 (repeat cycles 8–117) were edited and corrected as discussed by King et al. (1994) and Stammer and Wunsch (1994) with the following two exceptions that significantly improved the accuracy of the data (Shum et al. 1997, Tapley et al. 1997): first, we used the Version 3.0 ocean tide model provided by the University of Texas/Center for Space Research Group (Ma et al. 1994) to remove the ocean tide component from the SSH observations and, second, the standard orbits based on the JGM-2 geoid model (Nerem et al. 1994) were replaced by the improved estimates based on the recent JGM-3 geoid model (Tapley et al. 1996). No data from the French instrument were used because of enhanced noise levels in the Centre National d'Etudes Spatiales (CNES) altimeter (see also Fig. 8); earlier TOPEX cycles were omitted because of lingering questions about initial pointing errors of the T/P instrument. In practice, however, results with TOPEX cycle 2–7 included are indistinguishable from the ones shown here. Fu et al. (1994) provide details on the mission characteristics and its performance. Numerous recent studies demonstrated the high accuracy and precision of the T/P instrument, which are now at the 2–3 cm level (see the T/P special issues of *Journal of Geophysical Research* from December 1994 and December 1995). The spacecraft provides SSH observations with global coverage every 9.91 days (a nominal ''10-day'' ''exact repeat'' cycle) and with a horizontal alongtrack resolution of about 6.2 km.

Only the time variable SSH component is considered during this study, thus eliminating any uncertainties related to the geoid and the mean ocean state. A 3-yr alongtrack (local) mean was subtracted from each individual repeat cycle to produce its time variable part $\zeta(t)$ and its horizontal slope $\delta(t) = \partial\zeta/\partial l$, with l being the alongtrack distance. The data are subsequently split into areas spanning 10° in latitude and longitude on an overlapping 5° grid (Fig. 1) for which one-dimensional ensemble averages of ζ and δ spectra are computed in both the frequency and wavenumber domains. The spectra and their related autocorrelation functions are used subsequently to infer scales of ocean variability.

The paper is organized as follows in section 2 we discuss estimates of eddy kinetic energy derived from T/P data and its sensitivity to the applied filter length scale. Spectra are analyzed in section 3, and covariances and scales of oceanic variability are discussed in section 4. Their relation to the first-mode Rossby deformation radius L_{Ro} and an estimate of a ''Rhines'' scale L_{Rh} of the mean flow field are the basis of a dynamical interpretation given in section 5. A global description of surface variability in terms of universal wavenumber spectra and correlation functions is provided in section 6.

2. Eddy kinetic energy

Assuming a geostrophic balance and isotropic conditions, an estimate of the near-surface eddy kinetic energy K_E can be obtained from alongtrack sea surface height anomalies as

$$K_E = \langle v_s^2 \rangle, \tag{1}$$

where

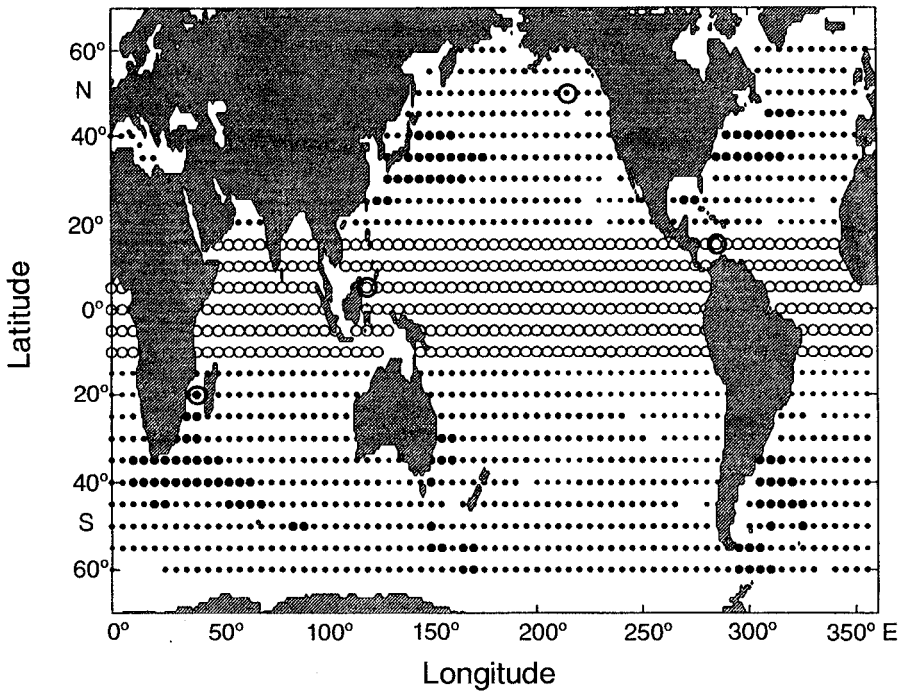

FIG. 1. The 5° by 5° grid on which spectra and scales of ocean variability were computed in overlapping areas, each spanning 10° on the side. Marked for later use are the tropical ocean (open circles), very low energy areas with $\gamma < 6$ cm (small dots), the bulk of the oceans with 6 cm $< \gamma <$ 15 cm (medium dots), and the high energy areas with $\gamma > 15$ cm. Bold circle mark locations of regional spectra shown in Figs. 8 and 9, from surface height ζ and slope δ, respectively.

$$v_s = -f^{-1}g\,\partial\zeta/\partial l \qquad (2)$$

is the surface geostrophic velocity component normal (positive eastward) to the local track orientation, and ζ and l the alongtrack SSH anomaly and northward coordinate, respectively. A corresponding K_E field is shown in Fig. 2 (plotted in $\log_{10}$ form) that results from the local cross-track velocity variance during the 3-yr period, and after averaging in 2° by 2° geographical boxes. Most prominent in the plate is the presence of very high kinetic energy in the Tropics, associated with the decreasing Coriolis parameter $f = 2\Omega\sin(\phi)$ toward the equator. Maximum amplitudes are located in the Indian Ocean, while the tropical Atlantic appear relatively low in variability (compare also Fig. 3 and Stammer et al. 1996).

In mid and high latitudes, T/P results are qualitatively similar to those from earlier studies (e.g., Shum et al. 1990; Le Traon et al. 1990; Beckmann et al. 1994) in that maximum amplitudes of K_E are associated with the paths of energetic current systems. In the interior ocean, the field exhibits zonally banded structures with areas of enhanced eddy activity following major mean fronts. T/P data, however, reveal regional details that previously were hidden in the noise or were removed by filters. In the present estimate, amplitudes of the background variability are of the order of 50 cm^2 s^{-2} in the eastern North Atlantic as compared to 100 cm^2 s^{-2} previously from Geosat, about 40 cm^2 s^{-2} in the South Pacific, and as low as 20 cm^2 s^{-2} in the northern North Pacific. However, exact numbers depend on details of the filtering, as discussed below.

Because Fig. 2 is dominated by the low-latitude bulk of the high eddy kinetic energy, much more detail in spatial structures can be seen from a field of an equivalent sea surface slope variability $K_{sl} = K_E\sin^2(\phi)$, shown in Fig. 3a. This field largely coincides in its spatial structure with those from small-scale SSH variability (potential energy) in which contributions from steric and other large-scale variability on wavelength exceeding 1000 km were removed by bandpass filtering (see Wunsch and Stammer 1995; Stammer 1997). Note that there are clear bands of enhanced surface slope variability present in the Indian Ocean and along the South Pacific intertropical convergence zone, roughly along 25°S. A structure similar to that in the Indian Ocean is likewise present in the global Semtner and Chervin model (Stammer et al. 1996), suggesting a major frontal, yet undocumented, structure at that location.

In Figs. 2 and 3a, regions of enhanced eddy kinetic energy appear to coincide with locations of mean frontal structures. This is most clearly suggested in the fundamental difference between the mean flow pattern and the variability of the North Pacific and North Atlantic. The North Atlantic Current and the associated enhanced

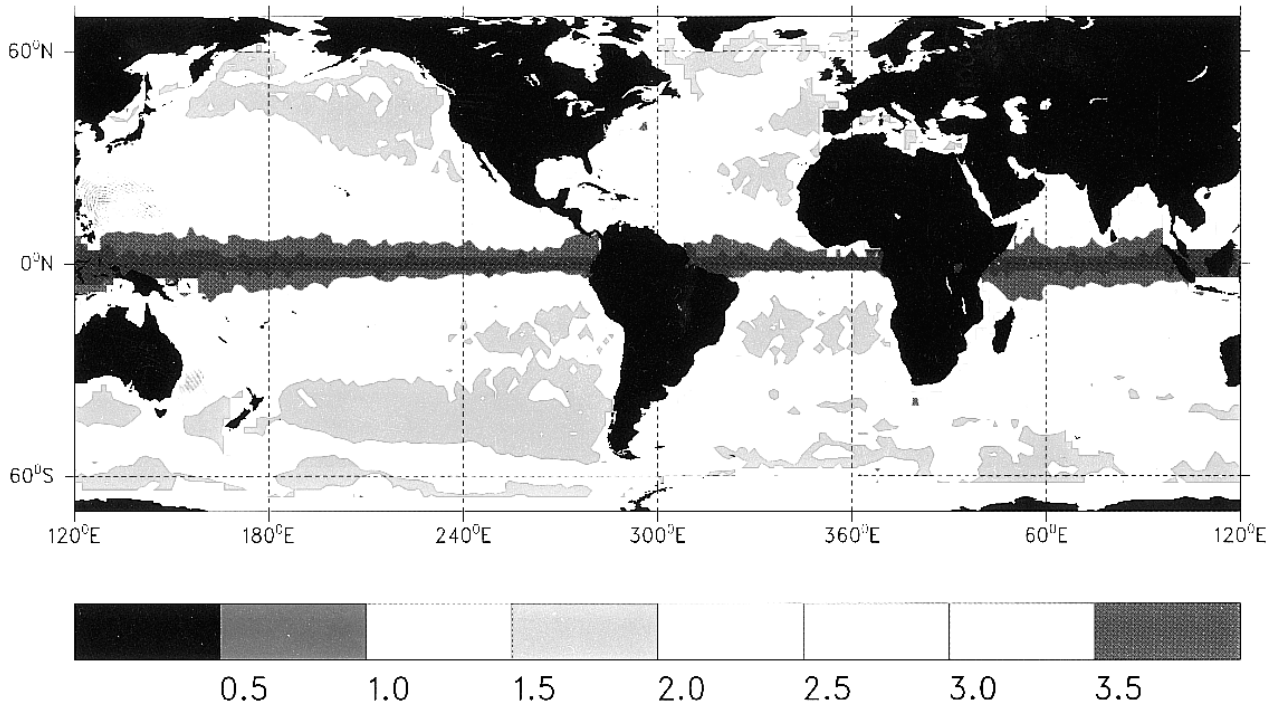

FIG. 2. Eddy kinetic energy, inferred from three years of TOPEX data (repeat cycle 8 through 117). Assuming isotropy, the field was constructed from cross-track geostrophic velocity. See the text for details on the computation. (Units are $cm^2\ s^{-2}$ and the field is plotted in $\log_{10}$ form.)

eddy energy reaches far into the European basin; equivalent structures in the mean flow field and eddy variability are completely missing in the North Pacific because of its different thermohaline circulation.

To emphasize an intriguing relation between the geographical distribution of K_E and horizontal density gradients embedded in the mean flow field, we show in Fig. 3b the kinetic energy $K_M = (\bar{u}^2 + \bar{v}^2)/2$ as it results from the mean thermal wind in 50-m depth relative to 1000 m in the Levitus climatology;

$$(\bar{u}, \bar{v}) = \frac{g}{\rho_0 f} \int_{-1000\,\mathrm{m}}^{-50\,\mathrm{m}} \left(\frac{\partial \rho}{\partial y}, \frac{\partial \rho}{\partial x} \right) dz. \qquad (3)$$

Results are plotted in Fig. 3b after scaling by $\sin^2(\phi)$, similar to the field in Fig. 3a. Not surprisingly, amplitudes of K_M are about an order of magnitude smaller than K_E (see, e.g., Wyrtki et al. 1976). But otherwise most of the areas characterized by enhanced eddy variability in T/P observations are characterized by enhanced mean horizontal density gradients and related mean kinetic energy in the upper thermocline. This holds also in the Southern Hemisphere along the aforementioned eddy variability ridges in the Indian Ocean and western Pacific along 25°S.

There are a few noteworthy discrepancies from this general tendency, especially in the vicinity of the East Australia Current, Brazil–Malvinas confluence, and the Agulhas Retroflection. There only weak mean baroclinic currents can be found, suggesting primarily barotropic fluctuations. Along the Antarctic Circumpolar Current (ACC), differences in K_E and K_M are primarily located close to topographic structures such as the Bollons Seamounts southeast of New Zealand (about 50°S, 183°E), or the Southwest Indian Ridge south of Africa (50°S, 30°E).

The close relation between the observed eddy variability and the mean horizontal density gradients is quantified in Fig. 4, showing a comparison of related amplitudes of the mean and the eddy velocity fields, $V_M = \sqrt{K_M}$ and $V_E = \sqrt{K_E}$, respectively. Both fields were previously averaged over 5° by 5° areas and result in a significant correlation of $r = 0.60$. A similar relation between the path of mean frontal structures and locations of enhanced eddy energy was previously recognized by Wyrtki et al. (1976) from ship drift data. Those authors discuss also the apparent decorrelation of high eddy activity with patterns of high atmospheric variability. These two findings are important ingredients for

→

FIG. 3. (a) As as in Fig. 2 but for an equivalent slope variance $K_{sl} = K_E \sin^2(\phi)$. Contour interval is 25 $cm^2\ s^{-2}$. (b) $K_M \sin^2(\phi)$ as it results from the thermal wind shear in 50-m depth relative to 1000 m in the Levitus climatology. Contour interval is 1 $cm^2\ s^{-2}$. See text for details.

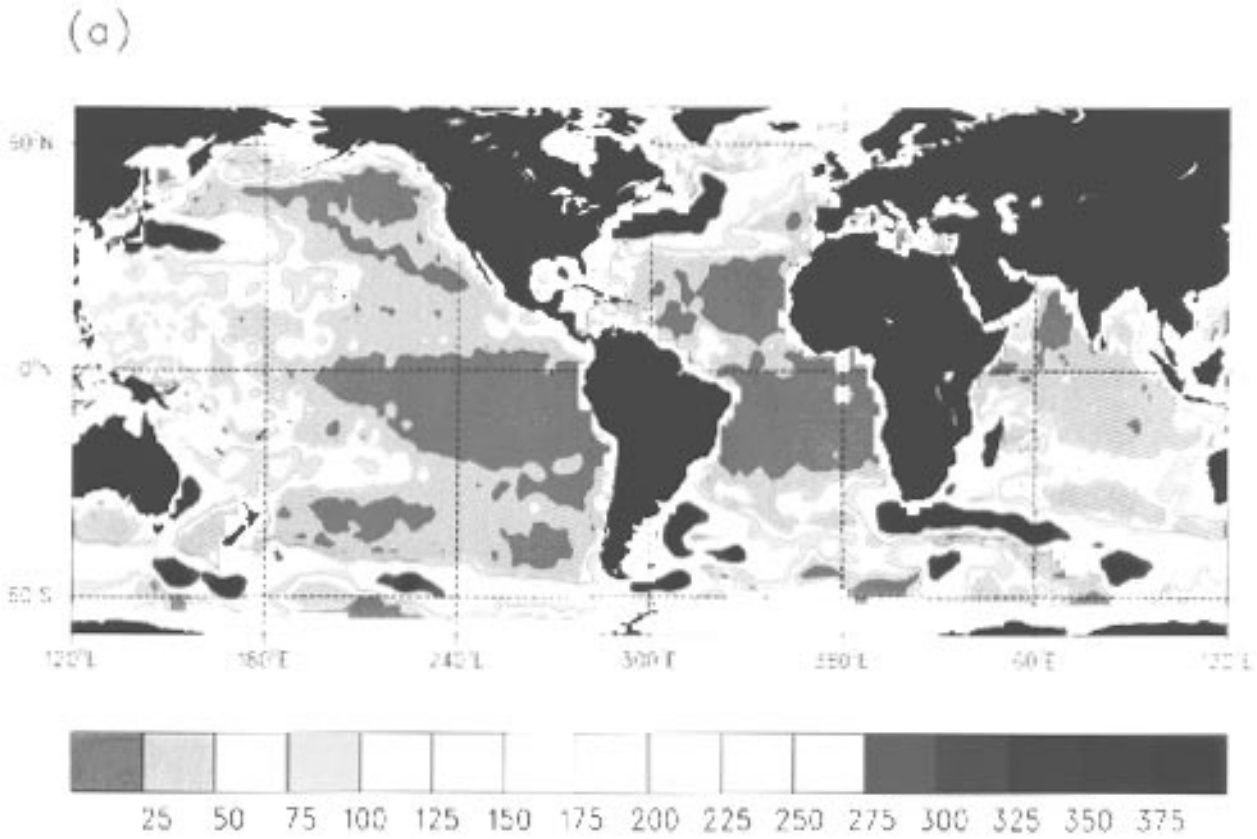
(a)
60°N
0°N
60°S
120°E
180°E
240°E
300°E
360°E
60°E
25 50 75 100 125 150 175 200 225 250 275 300 325 350 375

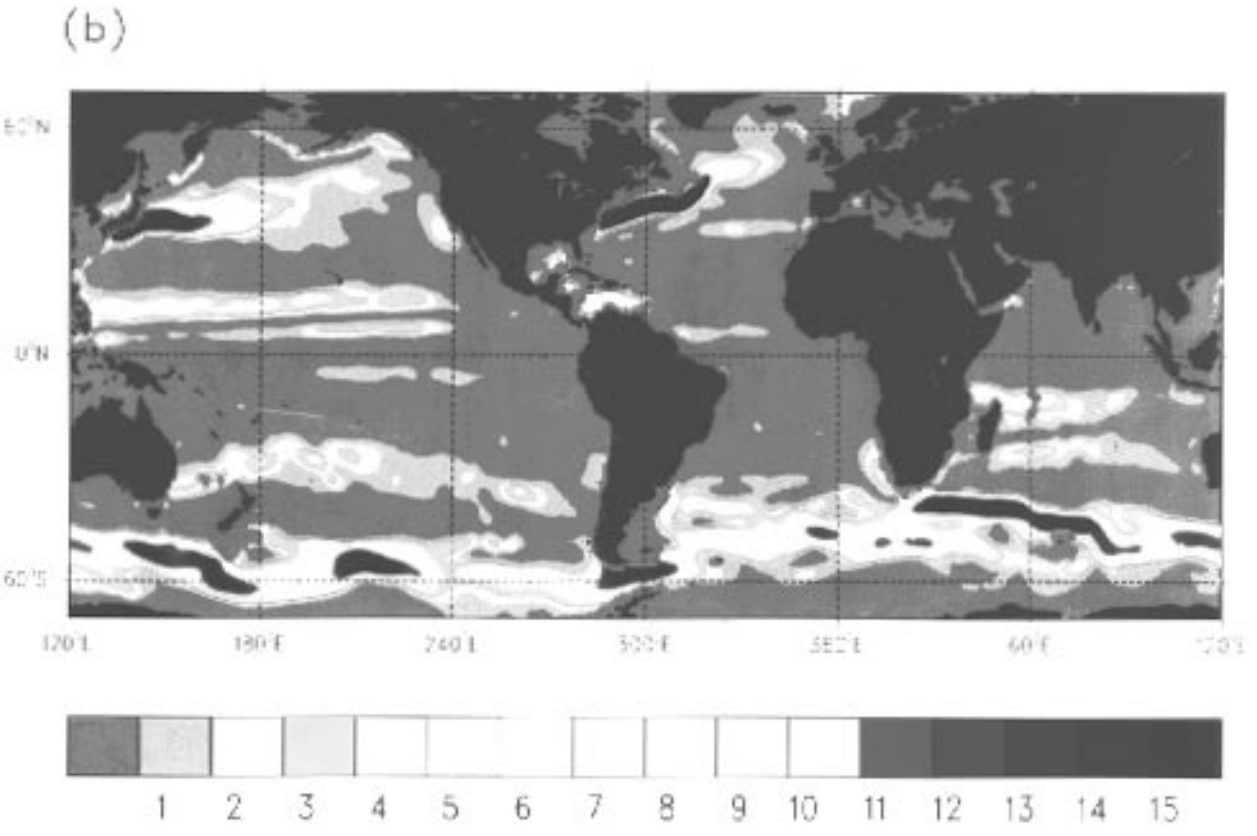
(b)
60°N
0°N
60°S
120°E
180°E
240°E
300°E
360°E
60°E
1 2 3 4 5 6 7 8 9 10 11 12 13 14 15

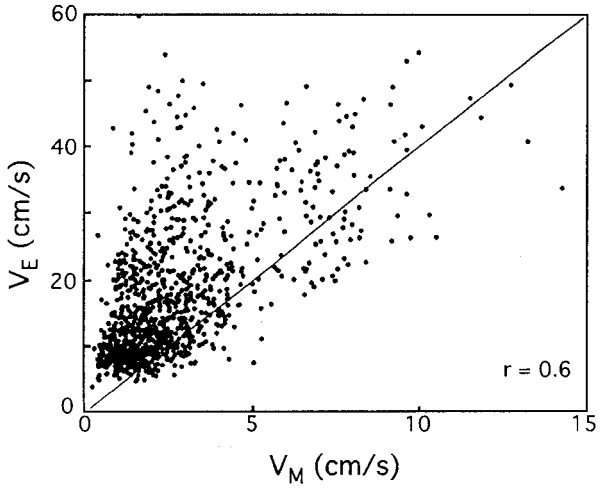

FIG. 4. Comparison of eddy velocity amplitudes $V_E = \sqrt{K_E}$ with the mean thermal wind in 50-m depth relative to 1000 m $V_M = \sqrt{K_M}$. Both variable are computed from fields shown in Figs. 3a, b poleward of 5° latitude, and after averaging in 5° by 5° areas. The correlation coefficient $r = 0.60$.

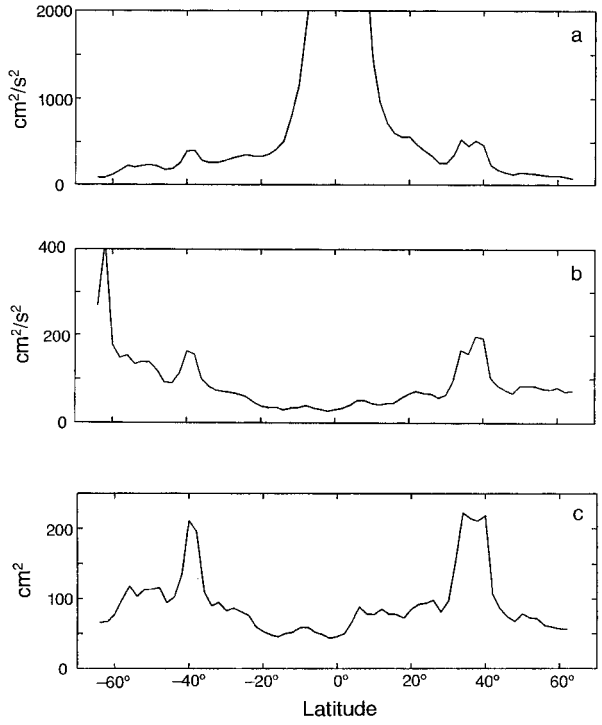

FIG. 5. Zonal averages between 0° and 360°E of (a) K_E, (b) K_{sl}, and (c) SSH variance, plotted against latitude.

a dynamical interpretation of observed eddy activity and its source mechanisms and strongly suggest internal instability processes (primarily baroclinic instability) to be a primary eddy source term as opposed to direct atmospheric forcing (see also the discussion in SB96). As will be discussed below, the latter term becomes important only where the general level of variability is low, for example, in the eastern North Pacific.

For many purposes a zonally averaged description of ocean variability appears useful. In Fig. 5, zonal averages between 0° and 360°E of K_E, K_{sl}, and SSH variance are provided as a function of latitude. In all three curves, high variability near 40°N and 40°S is associated with strong currents at those latitudes. But otherwise, the fields show interesting differences in their general latitudinal distribution. In terms of K_E, values decrease gradually from maximum amplitudes near the equator to minimum amplitudes in high latitudes. The opposite is true for K_{sl}, which is minimum in low latitudes and increases toward high latitudes. The SSH variability, on the other hand, is highest in mid latitudes [partly related to maximum contributions from seasonal steric effects in that latitude range (see Stammer 1997)], decreasing toward the poles and the equator. Note that both K_{sl} and SSH variance show a clear asymmetry with respect to the equator in that minimum amplitudes are located south of the equator, with considerably higher variability present at similar latitudes of the Northern Hemisphere associated with the North Equatorial Current (NEC) and the North Equatorial Countercurrent (NECC).

Filtering effects

Because the computation of v_s is equivalent to a high-pass filter, the noise component in the altimeter observations is enhanced by this operation. To reduce a noise contamination of velocity and K_E estimates, altimeter data were traditionally filtered alongtrack prior to the computation of v_s, over spatial scales of 100 km (e.g., Le Traon et al. 1990) or longer (Shum et al. 1990). Because of the pronounced decrease of spatial eddy scales toward high latitudes (see below), this filter process removes important oceanic energy there. To retain that signal, one could use a latitudinally dependent filter scale. It seems more plausible, however, to keep the filter scale small everywhere and instead correct the resulting K_E estimates for a noise contribution in the SSH data. This was done in Figs. 2 and 3a, where the alongtrack SSH data have been smoothed prior to the geostrophic computation by applying a Lanczos (1959) low-pass filter with a 30-km filter cutoff. A residual noise component in the K_E estimate (corresponding to $\lambda_c = 30$ km, below) was corrected subsequently, which was estimated from the slope variability as follows below.

In Fig. 6a, zonal averages of K_{sl} between 10° and 30°W are plotted as a function of latitude for filter cutoff wavelength varying between 18 and 100 km. But in contrast to Fig. 3a, no additional noise was corrected. To estimate a general noise level, we assume that the slope variance on scales of 60 km and above is real and that smaller-scale variance in low latitudes resides entirely in the noise component. Then slope noise amplitudes of $A_0 = 70$ cm^2 s^{-2} and $A_0 = 20$ cm^2 s^{-2} emerge in the region of minimum variance at 15°S from the variance surplus of estimates based on $\lambda_c = 18$ km and

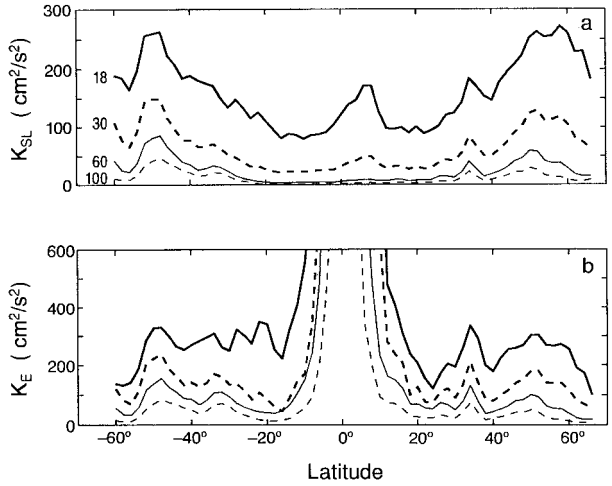

FIG. 6. (a) Equivalent slope variability $K_{sl} = K_E \sin(\phi)^2$, (cm^2 s^{-2}) zonally averaged between 20° and 40°W in the Atlantic. Curves correspond to Lanczos low-path cutoff wavelength of λ_c = 18 km (bold solid), 30 km (bold dashed), 60 km (thin solid), and 100 km (thin dashed), respectively. (b) Estimates of K_E (cm^2 s^{-2}) obtained from TOPEX/POSEIDON data for various filter length scales: 18 km (bold solid), 30 km (bold dashed), 60 km (thin solid), and 100 km (thin dashed). The first two estimates are corrected for a noise contribution of 70·sin^2 (ϕ) cm^2 s^{-2} and 20·sin^2 (ϕ) cm^2 s^{-2} in the filtered data.

λ_c = 30 km, relative to that with λ_c = 60 km, respectively. Although some minor fraction of this surplus is likely to be real, the assumption that it is completely noise related seems reasonable because eddy scales, increasing toward the equator, are longer than 60 km in low latitudes. Consistent with estimates by Fu et al. (1994) and an independent estimate from wavenumber spectra given below, the slope noise translates into an equivalent SSH noise amplitude of 1.5 cm (λ_c = 18 km) and 0.8 cm (λ_c = 30 km), respectively. Although small in high latitudes (about 20 cm^2 s^2), its contribution to K_E estimates would lead to vastly overestimated values in low latitudes (as high as 2700 cm^2 s^2 at about 5°) if not corrected by subtracting values of $A_0\sin(\phi)^2$ from the (filtered) K_E estimates. This was done in Fig. 2 and 3a, with A_0 = 20 cm^2 s^{-2}.

Figure 6b shows the resulting K_E estimates for λ_c of 18, 30, 60, and 100 km, respectively, with a noise effect corrected in the first two curves. Estimates of K_E from drifting buoys with drogues at 100-m depth (Brügge 1995; Schäfer and Krauss 1995) generally fall within the range resulting from λ_c = 18 and 30 km (see SB96). Note that more than 50% of K_E is present on spatial scales below 100 km in the figure.

The degree of spatial structures present in K_{sl} on wavelengths below 100 km is illustrated in Fig. 7, which shows maps of K_{sl} determined as the differences between individual fields obtained with filter cutoffs of 18 and 30 km, 30 and 60 km, 60 and 100 km, and 30 and 100 km, respectively (equivalent to differences between corresponding curves in Fig. 6b). (Note that the noise effect was corrected in the fields with λ_c = 18 and 30 km.) Instead of being spatially homogeneous in character, the slope variability down to 20 km is highly correlated with oceanic structures. As will become clearer below, eddy scales decrease toward high latitudes, and therefore different filter scales have a significant effect not only on the overall energy level but also on details in spatial pattern of K_E estimates. In particular, eddy energy in high-latitude locations such as the European basin and the Labrador Sea seems to be dominated by scales below 60 km. This is consistent with the pronounced decrease of the first-mode Rossby radius of deformation to below 10 km north of 50°N (compare Fig. 23).

3. Spectral analysis

Maps of ocean variability call one's attention to the pronounced inhomogeneous nature of the mesoscale and highlight regions of intense eddy variability and eddy mixing. But because oceanic variability is broadband, a detailed spectral analysis is required to fully understand its characteristics. Ultimately, regional two-dimensional frequency–wavenumber spectra are sought, equivalent to the global frequency–wavenumber spectrum in WS95. Because one-dimensional spectra are more common in the literature (and therefore easier to compare with previously published results), we will start here with a discussion of regional and globally averaged one-dimensional spectra that are obtained separately in the frequency and wavenumber domains. A similar discussion of ocean variability—but in its full two-dimensional form—is in preparation.

To compute frequency spectra of SSH variability $\zeta(t)$ and cross-track geostrophic velocity $v_s(t)$, local (along-track) time series from both ascending and descending arcs were Fourier analyzed to produce corresponding functions in frequency domain, $\hat{\zeta}(\sigma)$ and $\hat{v}_s(\sigma)$, and related periodograms; for example, $|\hat{\zeta}(\sigma)|^2$. Here σ has dimensions of cycles per second. Time series were tapered previously by using a cosine squared function over 10% of the number of observations. Gaps smaller than 20 days in time and 30 km in space were closed by interpolation, and data with larger gaps were rejected. To enhance statistical independency of results, periodograms were computed at only every second along-track position (every 12 km). Because in many cases the spectra of surface slope δ seems to be more appropriate than those of velocity, we show primarily slope spectra, which differ from the velocity spectra by a latitudinal dependent coefficient (but see Fig. 13).

Estimates of power spectral density of ζ and δ, $\Gamma_\zeta(\sigma)$ and $\Gamma_\delta(\sigma)$, were computed subsequently by ensemble averaging all individual periodograms present in individual 10° by 10° geographical areas. The number N of time series present in each region is typically about 500, which would result in a formal degree of freedom around N_{dof} = 1000, if all periodograms were truly independent.

Wavenumber spectra, $\Gamma_\zeta(k)$, were computed along

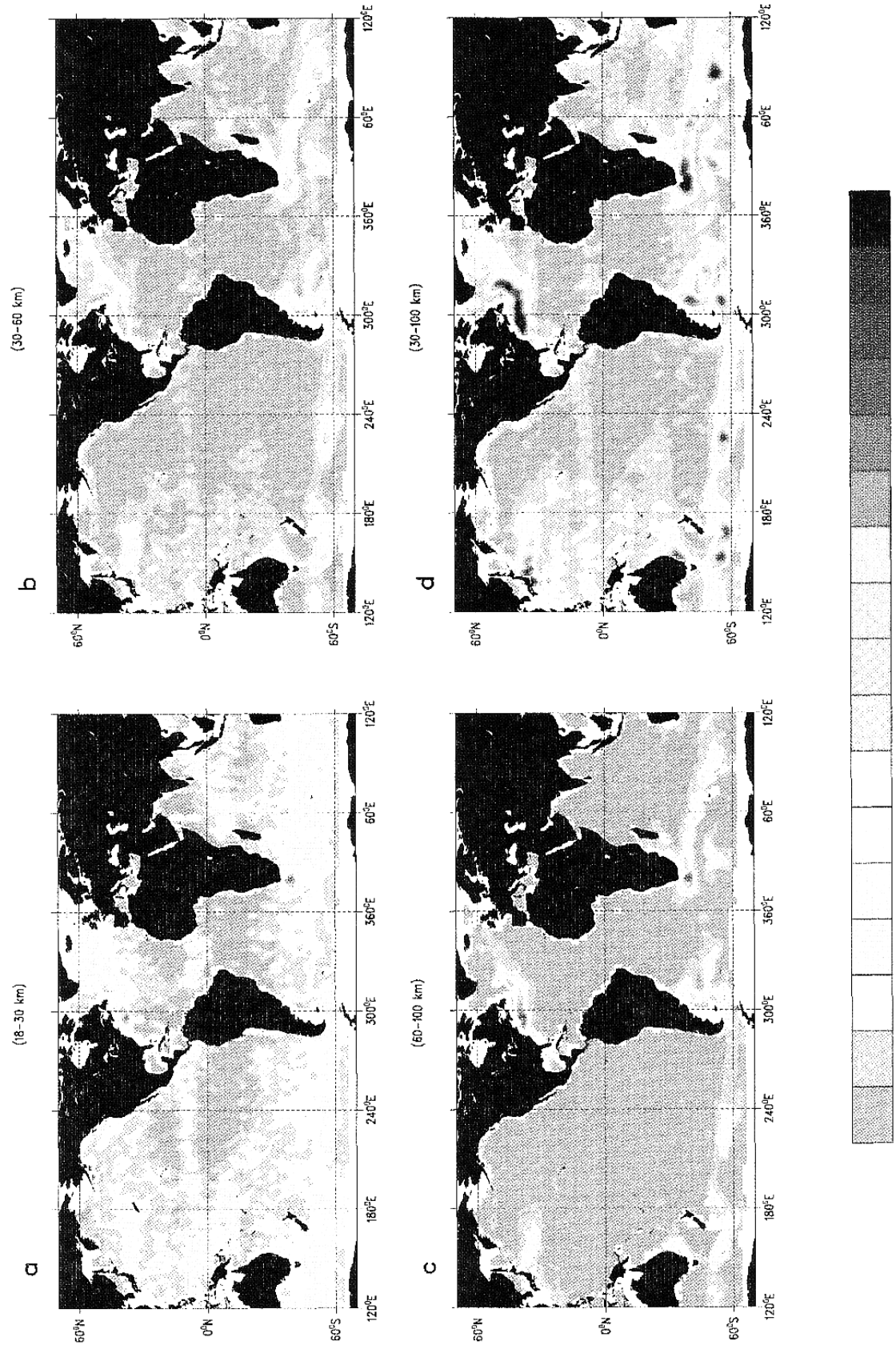

FIG. 7. $\Delta K_{sl} = \Delta K_s \sin^2(\phi)$ analyzed from the TOPEX data in the wavenumber ranges (a) 18–30 km, (b) 30–60 km, (c) 60–100 km, and (d) 30–100 km, respectively. These fields emerge as differences between individual fields, each computed from SSH data with a corresponding Lanczos low-path filter applied. Contour interval is 25 cm^2 s^{-2}.

those fractions of ascending and descending arcs that completely span individual 10° regions meridionally, with k being the alongtrack wavenumber. The length of each individual arc segment was required to be 180 × 6.2 km = 1110 km. The number N of valid data series, which is now the number of arcs times repetitions, is typically of the order of 500 in the interior oceans; close to boundaries, however, N becomes as low as 100.

As with computations in the frequency domain, wavenumber spectra can be computed for SSH and surface slope. Because of the geostrophic relation, slope and velocity wavenumber spectra are readily obtained from the height spectra as

$$\Gamma_\delta(k) = (2\pi k)^2\Gamma_\zeta(k) \tag{4}$$

and

$$\Gamma_u(k) = \frac{g^2}{f^2}(2\pi k)^2\Gamma_\zeta(k), \tag{5}$$

respectively, with g being the gravity constant and f, as before, the Coriolis parameter. Results are similar in detail, and most of what follows is based on the latter equation, with the advantage that filtered slope spectra are available once filtered versions of $\Gamma_\zeta(k)$ are provided (see below).

An alongtrack spectrum can be converted into an isotropic scalar wavenumber spectrum (e.g., Fu 1983; see also Le Traon et al. 1990). However, because alongtrack spectra are more common in the literature, we will continue to work with that form. To the extent that spectral relations in Fu (1983) did not change significantly upon the transformation, conclusions drawn here appear insensitive to the specific representation.

a. Global-averaged spectra

We begin with a discussion of those global frequency and wavenumber spectra that result from averaging height and slope spectra from all individual subregions over the World Ocean.

The global-average SSH frequency spectrum, $\bar{\Gamma}_\zeta(\sigma)$, (Fig. 8a) is largely consistent with the earlier estimate in WS95 (their Fig. 4a) but shows a few important modifications, including a substantially smaller contamination by residual tidal constituents (near 60-day periods) as a result of the improved tide model used in this study. Maximum energy is found at the annual period superimposed on a background energy distribution, which roughly follows a $\sigma^{-1/3}$ relation at periods longer than 250 days. Toward shorter timescales, the decrease follows a σ^{-1} relation as before, but at about a 30-day period there is now a break toward a σ^{-2} decay, not present in the earlier estimate. As indicated in the figure from a spectrum that includes data from the CNES instrument over the same period (thin line), the primary source for the steeper short period decay in this new result has to be considered the decreased noise contamination by the omitted POSEIDON data. A similar conclusion is reached from $\Gamma_\zeta(k)$, $\Gamma_\delta(\sigma)$, and $\Gamma_\delta(k)$, respectively (Figs. 8b–d)

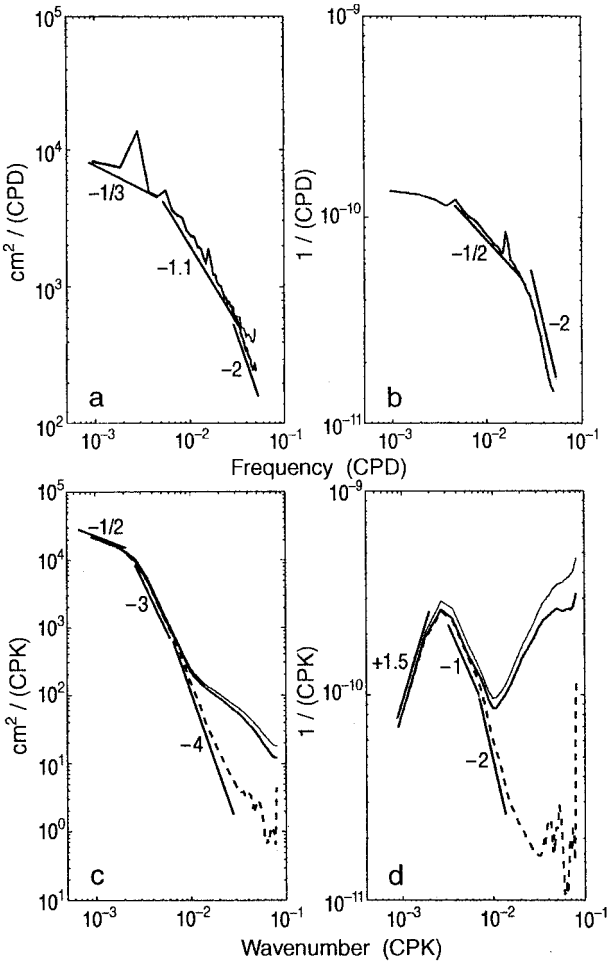

FIG. 8. Global-averaged frequency spectrum of (a) sea surface height and (b) sea surface slope. In both cases the bold lines are based entirely on TOPEX data, and thin lines indicate results with POSEIDON data included. (c) Global-averaged wavenumber spectrum of sea surface height and (d) sea surface slope. Bold solid lines show the initial spectra based on TOPEX data, and thin lines include POSEIDON data. Bold dashed lines give results after applying an optimal filter. See text and Fig. 11 for details on the filter. Total variance associated with the curves is 93.8 cm², 2.97 × 10^{-12} cm²/cm², 50.9 cm², and 3.06 × 10^{-12} cm²/cm², for (a), (b), (c), and (d), respectively.

The global-mean slope spectrum, $\bar{\Gamma}_\delta(\sigma)$, roughly follows a $\sigma^{-1/2}$ relation for periods between 40 and 250 days, with an almost ''white'' long-period plateau and a σ^{-2} relation on shorter periods, respectively. Again, the peak around 60 days still has to be interpreted as a contamination by a residual tidal contribution.

Globally averaged wavenumber spectra of ζ and δ are shown in Figs. 8c and 8d (thin lines; for a discussion of the bold lines see below). Those figures are similar to Figs. 9b and 10 in WS95 except that energetic boundary currents are much better represented now, resulting in an overall energy increase by roughly a factor of 2

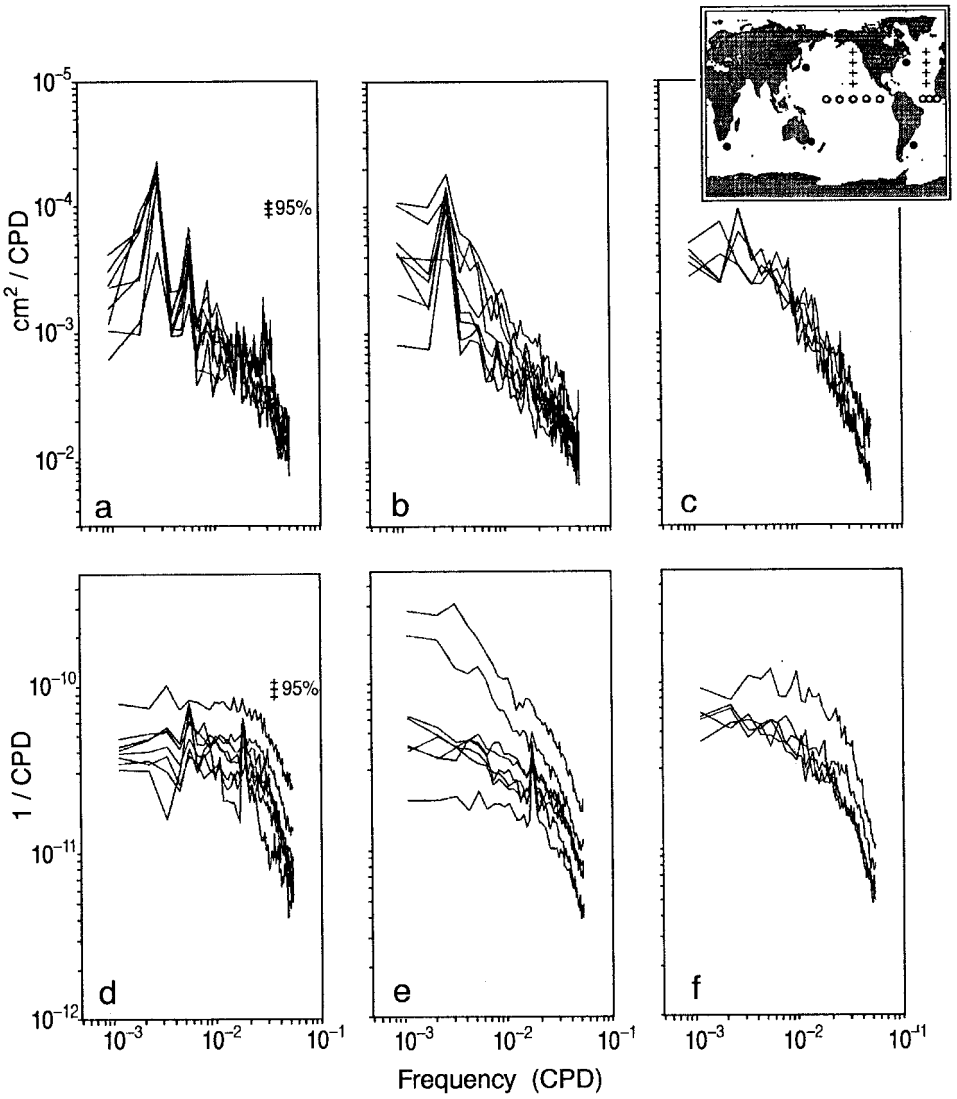

FIG. 9. Regional frequency spectra of sea surface height (a–c) and surface slope (d–f) from (a,d) high-energy boundary current regions, (b,e) the interior oceans, and (c,f) the tropical oceans. Positions of individual spectra are marked in the inset.

to 51 cm² over the previous estimate. In terms of simple power laws, the $\bar{\Gamma}_\zeta(k)$ spectrum roughly follows relations of $k^{-1/2}$ at wavelengths longer than 350 km, of k^{-3} for $100 < k^{-1} < 350$ km, and $k^{-3/2}$, at shorter wavelength. Equivalently, the surface slope spectrum, $\bar{\Gamma}_\delta(k)_i$ can be summarized by $k^{+1.2}$ and k^{-1} relations on wavelength longer and shorter than 350 km, respectively. For a discussion of the small-scale part of the spectrum and its noise contamination see below.

The power laws stated here are provided as simple reference relations for the globally averaged spectra. Because these spectra characterize a mixture of dynamics distributed geographically over the World Ocean and over a wide range in frequencies and wavenumbers space, no dynamical significance should be attached to them at this point. A discussion on dynamics will be given below based on regional studies.

b. *Regional frequency spectra*

Regional variations present in SSH frequency spectra $\Gamma_\zeta(\sigma)$ are summarized in Fig. 9, which shows typical spectra from three dynamically distinct regions—1) the tropical oceans, 2) the bulk of the interior oceans, and 3) the energetic boundary currents—with geographical locations of individual spectra indicated in the figure inset. Frequency spectra of the related slope fields δ, which allow a direct comparison with results from moored current meter data, are given in Figs. 9d–f from the same geographical locations. The slope spectra were

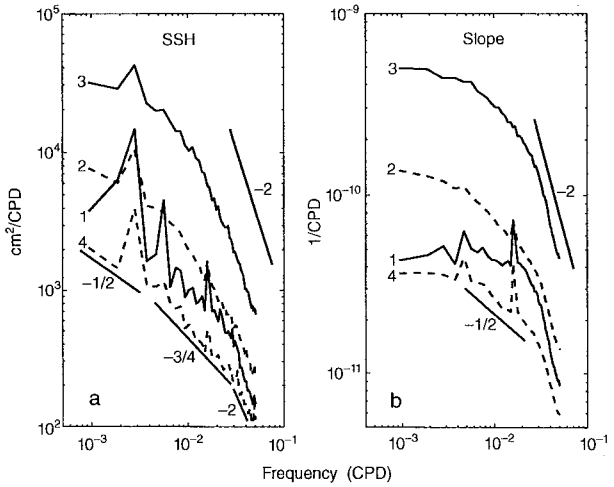

FIG. 10. (a) Averaged frequency spectra from 1) the Tropics, 2) the bulk of the global ocean, 3) the high energy areas, and 4) the very low energy areas, respectively. The geographical distribution of those regions is marked in Fig. 1 by open circle, medium, bold, and small dots, respectively. (b) As in (a) but for the alongtrack slope component.

estimated from the T/P data after alongtrack smoothing with a 30-km filter scale. Varying that scale between 20 to 100 km does not alter the general structure but tends to make slopes slightly steeper for long wavelength filter cutoffs.

Most striking in Fig. 9 is the pronounced similarity in shape of all spectra from each dynamical category. This is particularly clear from $\Gamma_\zeta(\sigma)$. Apart from a few exceptions, it holds for both $\Gamma_\zeta(\sigma)$ and $\Gamma_\delta(\sigma)$ over the entire World Ocean. Accordingly, three basic types of $\Gamma_\zeta(\sigma)$ and $\Gamma_\delta(\sigma)$ spectra can be identified from an inspection of individual spectra from all 10° subregions. In combination with the local energy level, those spectra give a first-order description of observed fluctuation in sea surface height and surface slope in the frequency domain. Corresponding curves in Fig. 10 represent 1) all of the tropical oceans between 5°S and 15°N, 2) the bulk of the oceans characterized by an rms SSH variability 6 cm $< \gamma <$ 15 cm, and 3) the high energy areas with $\gamma >$ 15 cm. These three regions are marked in Fig. 1 by open circles, medium dots, and bold dots, respectively.

In accordance with previous studies (e.g., Patullo et al. 1955 and Gill and Niiler 1973), all individual sea surface height spectra show a pronounced peak at the annual period, on top of a $\sigma^{-1/2}$ long-period relation. In mid and high latitudes, the associated SSH variability is primarily related to the local (dynamically passive) expansion and contraction of the water column as a result of seasonal surface heat flux variations (see also Stammer 1997), while in low latitudes (Fig. 9c), wind stress fluctuations and related current changes are the primary cause for SSH variations at the annual period (Philander 1978).

In the tropical regime (#1 in Fig. 10a) a second peak is present at the semiannual frequency superimposed on a continuous $\sigma^{-1/2}$ decay, which characterizes the spectrum at periods between 30 and 200 days. A further peak apparent in Fig. 9a around 30-day periods is related to instability waves in the eastern tropical Pacific (Philander 1990; see also Périgaud 1990; Plate 6 in Busalacchi et al. 1994; and McPhaden 1996).

In the interior ocean the general shape of the SSH spectrum (#2 in Fig. 10a) basically agrees with the global average shown in Fig. 6a but with about 25% less energy. Note that its spectral decay is close to $\sigma^{-3/4}$ (Fig. 9b), a relation also found in numerical simulations of geostrophic turbulence (McWilliams and Chow 1981).

In the high-energy regions (#3 in Fig. 10a) on the other hand, a significantly different behavior from the previous two regimes is found in that energy stays high at periods longer than about 100 days and follows a steep σ^{-2} relation toward shorter periods. Wunsch (1972) reported a similar spectral decay at periods less than 80 days from Bermuda tide gauge records (compare also Vasquez et al. 1990).

A further spectrum (#4 in Fig. 10a), representing the very low energy areas with $\gamma <$ 6 cm (small dots in Fig. 1), can be considered a transition from tropical to midlatitude conditions. It shows a $\sigma^{-3/4}$ relation at periods between 30 days and a year. At even short periods all four curves lead into a σ^{-2} tail.

In terms of averaged slope spectra (Fig. 10b), the most striking differences are present at long periods where the estimate from the Tropics (#1) shows basically a ''white'' energy distribution at periods longer than about 60 days. In contrast, spectra from the interior ocean and the energetic regions show a ''red'' distribution over the full spectral range, with an intermediate $\sigma^{-1/2}$ regime and a short-period σ^{-2} decay. Those latter slope characteristics, with a flat low-frequency part and a steeper decay at higher frequencies appear qualitatively consistent with results from moored current meter data (cf. Wunsch 1981, 1997; Müller and Siedler 1992; Schmitz and Luyten 1991). Altimetry, however, suggests a more moderate decay than inferred from subsurface mooring data, which typically follows a σ^{-2} relation at periods less 100 days. The extent to which this difference is related to the influence of surface-trapped signals not present in the mooring data needs further attention.

Although deviations from those basic spectra exist, the locations of largest anomalies are generally confined to the boundaries of the oceans. A few examples are given in Figs. 11 and 12, showing Γ_ζ and Γ_δ spectra from (a) the Indian Ocean at 15°S, 54°E; (b) the western tropical Pacific at 5°N, 125°E, the North Brazil Current region at 15°N, 75°W, and the eastern North Pacific at 45°N, 220°E. In the Indian Ocean and in the North Brazil Current region, there is a pronounced energy excess in Γ_ζ near 60-day periods because of eddy shedding (Did-

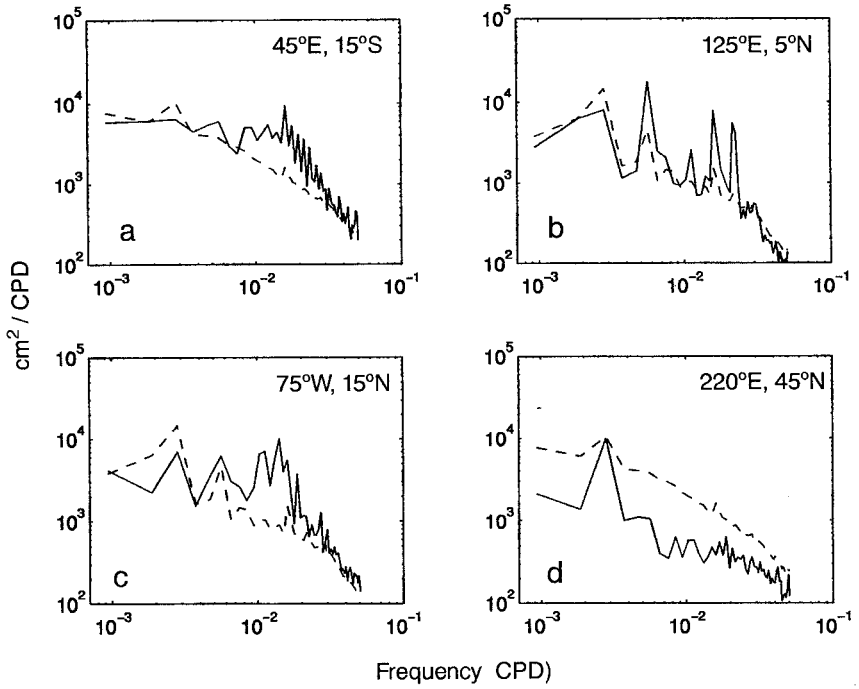

FIG. 11. Regional SSH frequency spectra $\Gamma_\zeta(\sigma)$ from a few locations marked in Fig. 1 by bold circles: (a) 15°S, 45°E; (b) 5°N, 125°E; (c) 15°N, 75°W; and (d) 45°N, 220°E. Dashed curve show the mean spectra for the corresponding regions as reference.

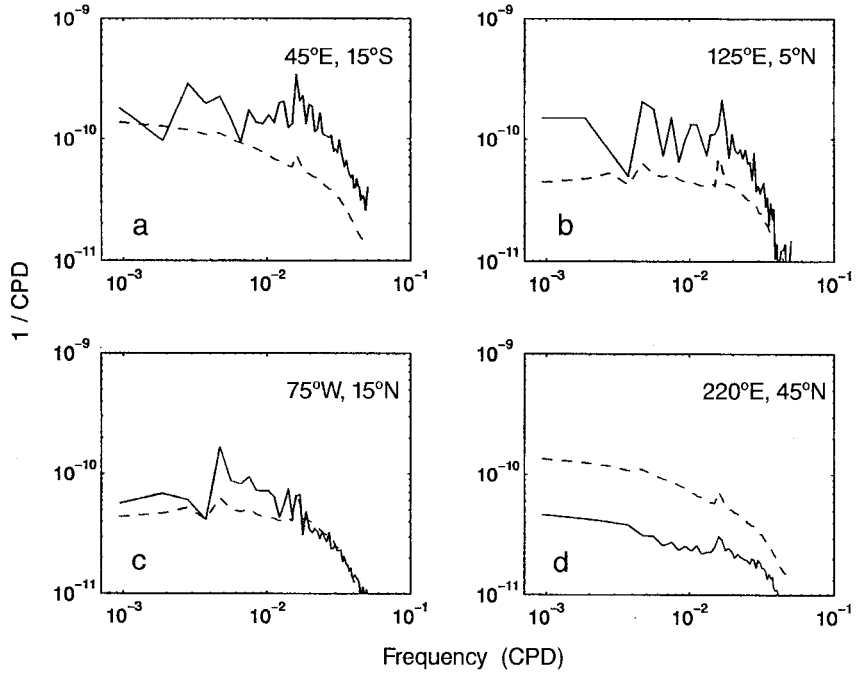

FIG. 12. As in Fig. 8 but for slope frequency spectra $\Gamma_\zeta(\sigma)$.

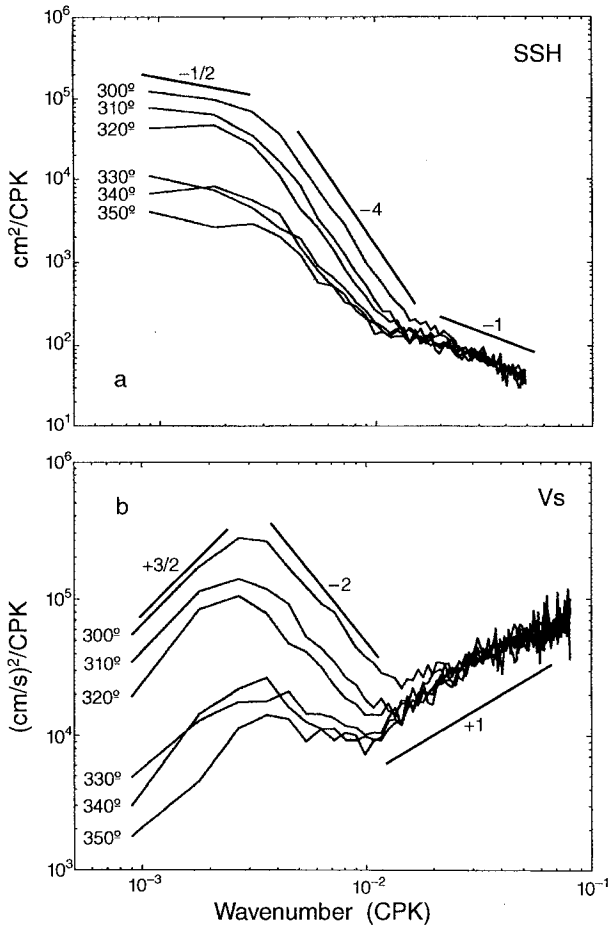

FIG. 13. TOPEX/POSEIDON mean alongtrack wavenumber spectra for (a) sea surface height and (b) cross-track velocity from various 10° × 10° areas between 30° and 40°N with center longitudes indicated in the figure.

den and Schott 1993; Richardson et al. 1994). In the western tropical Pacific, enhanced energy appears in the Γ_ζ spectrum at specific bands that are strikingly close to tidal aliasing frequencies. They are therefore likely to be related to enhanced residual tidal errors at that location. In the eastern North Pacific at 45°N, 220°E, on the other hand, energy is missing at most frequencies except at short periods associated with barotropic wind-induced fluctuations.

c. Wavenumber spectra

Examples of regional ζ and v_s wavenumber spectra, $\Gamma_\zeta(k)$ and $\Gamma_u(k)$, are shown in Fig. 13 from several 10° by 10° areas in the latitude band 30° to 40° N across the North Atlantic. As can be expected from a nearly isotropic eddy field (see Krauss and Böning 1987; Schäfer and Krauss 1995), spectra computed individually from ascending and descending arcs do not differ significantly from each other and are therefore not shown here separately.

Generally, the regional wavenumber spectra are consistent with the global estimates, but depict the pronounced geographical variation of eddy variability in the ocean. As a result, the energy in $\Gamma_\zeta(k)$ and $\Gamma_u(k)$ on wavelengths longer than about 100 km substantially increases from the eastern and central low-energy subtropical gyre toward the eddy-active boundary current regime of the North Atlantic. But apart from this, the general shape of individual spectra appear strikingly similar across the entire basin. All $\Gamma_\zeta(k)$ curves exhibit a long-wavelength plateau and a spectral break at about 400-km wavelength, followed by a drop in energy close to a k^{-4} relation. Associated velocity spectra have a maximum in energy at the above cutoff wavelength, with roughly $k^{+1.5}$ and k^{-2} relations toward longer and smaller wavelength, respectively.

Most remarkable in the figure is that both types of spectra lead into a unique high-wavenumber tail, which in terms of $\Gamma_\zeta(k)$ can be described by a $k^{-2/3}$ behavior. As indicated in Figs. 8c,d this finding holds over the entire World Ocean, and there are strong reasons to believe that this short wavelength tail of the spectrum is dominated by noise rather than ocean signal. Apart from the suspicious universal character over a highly inhomogeneous ocean, the breakdown of a geostrophic assumption at those very short spatial scales is another reason. Miscalibration is also an important source of uncertainty on wavelength smaller than 60 km (Rodriquez and Martin 1994). The ''noise'' in T/P data is also made up from a variety of complex and unknown contributions from environmental and geophysical corrections. At the present level of measurement accuracy, it also includes physical ocean processes that are not the subject of this study, such as the expression of internal wave and internal tide signals at the sea surface (Radok et al. 1967; Wunsch and Gill 1976). In terms of surface velocity and sea surface slope, the noise tail is responsible for their unphysical ''blue'' wavenumber energy distribution, which, on global average, leads to the peculiar bimodal energy in the slope spectrum (Fig. 8d).

1) OPTIMAL FILTER DESIGN

Because our present attempt is to relate observed energy distributions to underlying physical processes, it is essential to obtain reliable estimates of spectral slopes. To reduce noise contamination, we apply a filter to the wavenumber spectra prior to any further analysis. Press et al. (1992) give a useful introduction into the concept of an optimal filter.

Our goal is to analyze a spectrum $\check{\Gamma}_\zeta(k)$ of the true signal $\zeta(t)$. Our task is then to find a filter $\Phi(k)$, which when applied to the corrupted spectrum $\Gamma_\zeta(k)$, produces a best estimate $\tilde{\Gamma}_\zeta(k)$ that is as close as possible to the true spectrum:

$$\tilde{\Gamma}_\zeta(k) = \Gamma_\zeta(k)\cdot\Phi(k). \tag{6}$$

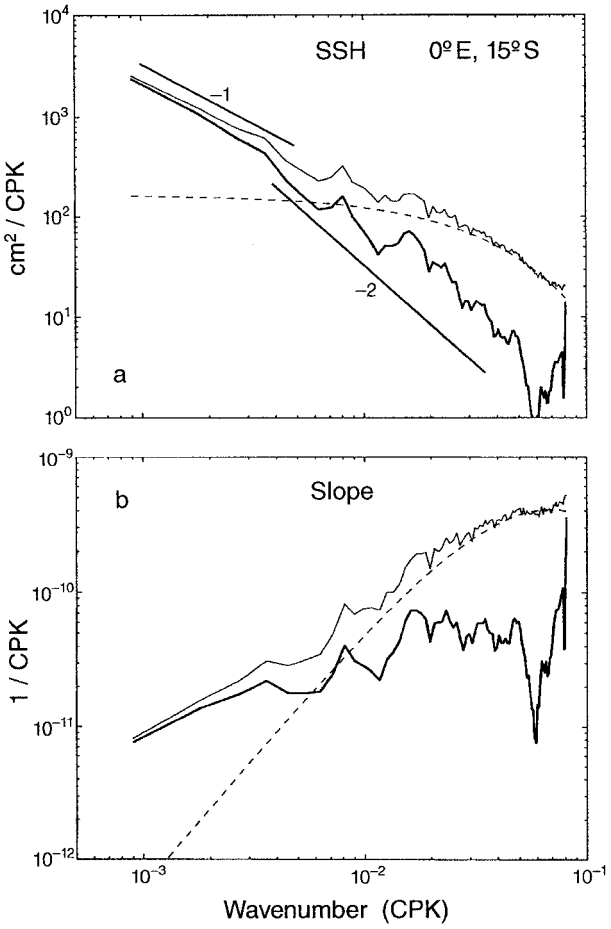

FIG. 14. Optimal filter design in the area centered at 15°S, 0° in the Atlantic Ocean. In (a) the thin, bold, and dashed lines are raw $\Gamma_\zeta(k)$ spectrum, filtered $\check{\Gamma}_\zeta(k)$ spectrum, and noise spectrum $N(k)$, respectively. In (b) similar results are shown, but for surface slope δ.

The underlying assumption is that the signal ζ and the noise n are uncorrelated. An optimal least-squares filter solution is given by (Press et al. 1992)

$$\Phi(k) = \frac{\check{\Gamma}_\zeta(k)}{\check{\Gamma}_\zeta(k) + N(k)} = \frac{\Gamma_\zeta(k) - N(k)}{\Gamma_\zeta(k)}. \qquad (7)$$

To construct the filter, some prior knowledge of the noise spectrum $N(k)$ is required, but adequate information on the noise statistics is not now available from the T/P Project. Under such conditions, a noise spectrum is usually determined empirically from the data itself. This was accomplished here by fitting a smooth curve to the high-wavenumber part of Γ_ζ obtained from the area of global minimum variance, centered at 15°S, 0°E in the South Atlantic (dashed line in Fig. 14). As before, we assume that all short-scale energy is purely noise related in this specific minimum variance location—a reasonable assumption under present conditions. Future refined applications clearly call for detailed information on the T/P error spectrum.

Using the dashed curve in Fig. 14a as a noise estimate of $\tilde{N}(\sigma)$ in (7), (6) then leads to the spectral estimate $\bar{\bar{\Gamma}}_\zeta(k)$ (bold line), which is unaltered at long wavelengths, but shows an increased decay close to k^{-2} toward short scales as compared to k^{-1} previously. In this specific example, the filter process reduces the total variance by about 50% from (2.8 cm)^2 to (2.0 cm)^2, leaving (1.9 cm)^2 as the noise estimate, a number consistent with the noise estimates in section 2 and with Fu et al. (1994). On the global average, about 7% of the variance is removed from the raw data by the filter process; but in high energy areas, the noise component amounts only to 1% of the observed variance. Note that the associated surface slope spectrum, $\Gamma_\delta(k)$, is changed by the filter process from completely ''blue'' into ''white,'' with all short-scale energy reduced by more than a decade (Fig. 14b).

2) FILTERED WAVENUMBER SPECTRA

To produce filtered spectra on the complete global grid, $\hat{\Gamma}_\zeta(k)$ follows from (6) with (7) evaluated in each of the 10° areas and with the above $\tilde{N}$ from the minimum variance area used as a general noise estimate. The resulting global average filtered spectrum $\bar{\bar{\hat{\Gamma}}}_\zeta(k)$ (bold line in Fig. 8c) shows a steepened spectral decay of about $k^{-3.3}$ between the 350-km cutoff and 20-km wavelength. In the mean slope spectrum $\bar{\bar{\hat{\Gamma}}}_\delta(k)$, the ''blue'' short-wavelength part has been completely removed; instead the energy follows now a k^{-1} relation at wavelengths between 400 and 150 km, and a k^{-2} relation at shorter wavelengths.

To facilitate a comparison of wavenumber spectra from various dynamically distinct regimes of the World Ocean, filtered spectra $\tilde{\Gamma}$ were subsequently normalized by their local variance γ^2 to produce spectra in *normalized* form

$$\hat{\Gamma}_\zeta(k) = \frac{1}{\gamma_2}\tilde{\Gamma}_\zeta(k). \qquad (8)$$

They are shown in Fig. 15 from all 10° areas on the 5° grid along various latitude bands spanning the complete sphere in both hemispheres, thus sampling all ocean basins. The figure reveals the unexpected result that, with the geographical variations in eddy energy removed from the spectra, all resulting curves of $\hat{\Gamma}_\zeta(k)$ are to first order similar in shape. Some regional deviations from this general behavior are evident but are mostly confined to the eastern North and South Pacific (Figs. 15a,b), where a relative high long-wavelength energy component is apparent that can be associated with barotropic (wind driven) fluctuations (see Chao and Fu 1995 and Fu and Davidson 1995).

In contrast to extratropical conditions, spectra from the tropical oceans are ''red'' over the full scale range and show a $k^{-2.5}$ relation at all wavelength exceeding 100 km. However, two limiting factors of the present analysis have to be considered. First, it is likely that residual noise effects are still present in low-energy

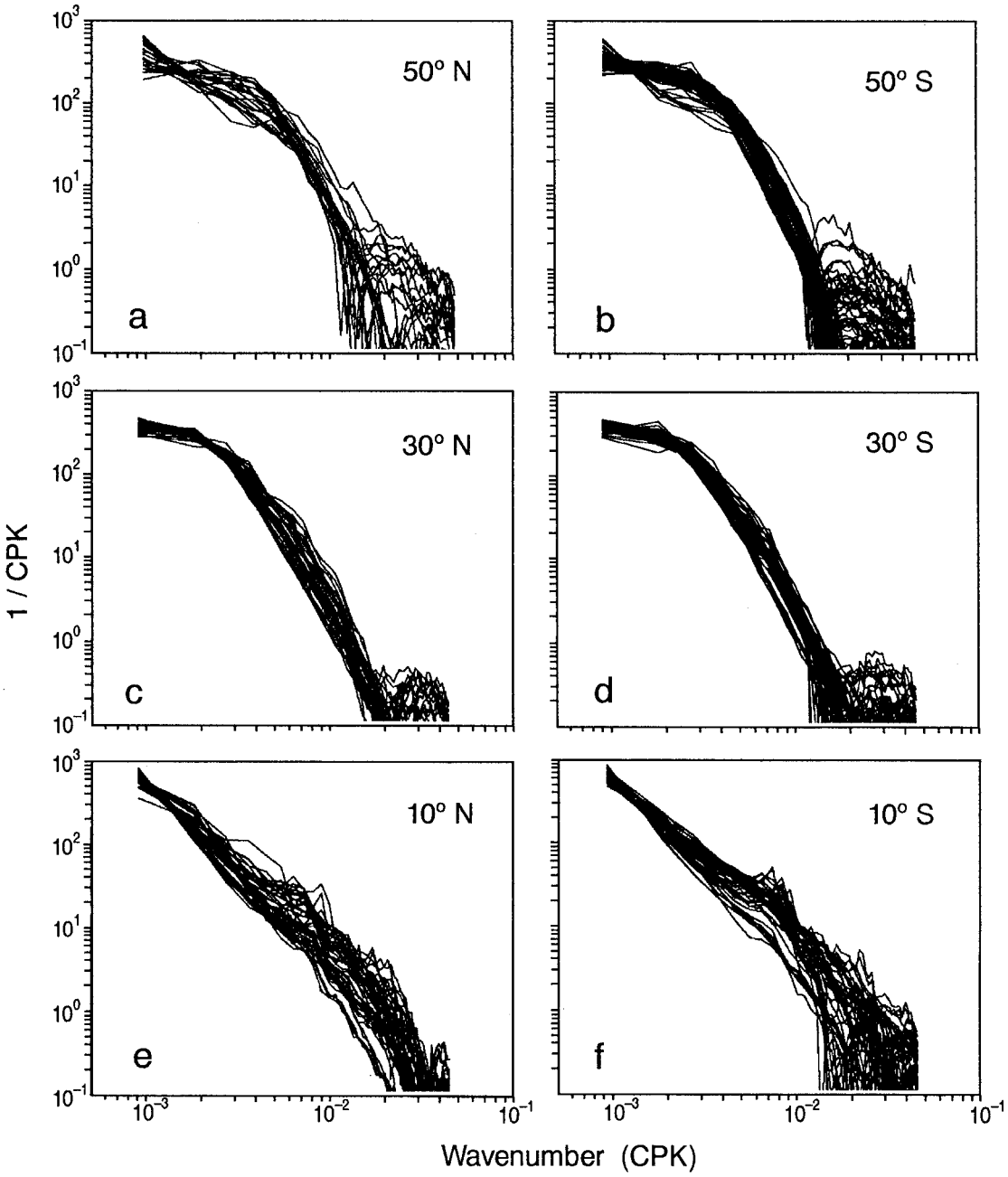

FIG. 15. Regional wavenumber spectra $\hat{\Gamma}_\zeta(k)$ after optimal filtering and after normalization by regional variance. Shown are spectra from all subregions along the zonal swaths centered at (a) 50°N, (b) 50°S, (c) 30°N, (d) 30°S, (e) 10°N, and (f) 10°S.

regions. More important, though, is that the geographical extent over which spectra are evaluated is becoming too small to resolve the long scales in low latitudes. Going from a 10° to 20° box size indeed leads to a spectral plateau at the longest wavelength, even in the Tropics (not shown, but see Stammer and Böning 1992). Some tropical locations exhibit enhanced energy at wavelengths around 110 km (Atlantic and Indian Ocean) and 150 km (western Pacific). The origin of those features—which are apparent north and south of the equator and which has been observed previously in Geosat data (Stammer and Böning 1992)—is not obvious and needs further attention. Because the Tropics are largely governed by different physics and because our main focus is on midlatitudes, we will not go into further details of low-latitude spectra. Instead we will limit the following discussion on dynamics to regions poleward of 15° latitude.

To emphasize the meridional variation in spectral

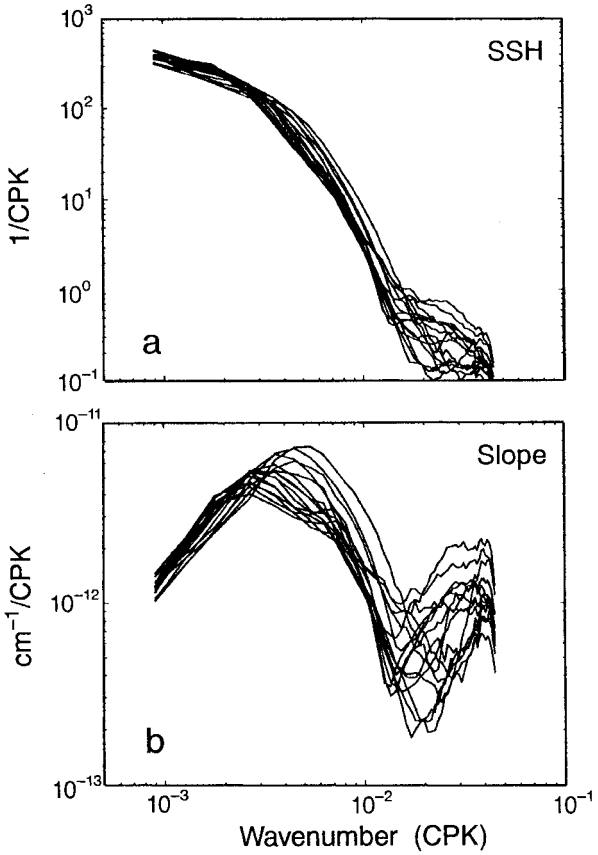

FIG. 16. Zonally averaged $\langle\hat{\Gamma}_\zeta\rangle(k)$ (a) and $\langle\hat{\Gamma}_\delta\rangle(k)$ spectra (b) shown for latitudes poleward of 20°.

shape, Fig. 16a shows mean $\langle\hat{\Gamma}_\zeta\rangle$ spectra that result from a zonal averaging around each latitude band on the 5° grid poleward of 20° latitude in both hemispheres. The figure illustrates the striking similarity among extratropical wavenumber spectra. All $\langle\hat{\Gamma}_\zeta\rangle$ curves show a close to universal $k^{-1/2}$ long-wavelength plateau and a steep decay of roughly k^{-4}. However, the cutoff wavenumber k_0 exhibits a latitudinal dependency by decreasing from high latitudes toward the equator. This meridional shift in the cutoff wavenumber is even more obvious from the slope spectra (Fig. 16b), which show a maximum energy at the wavenumber k_0 followed by a drop in energy similar to a k^{-3} relation.

Note that this general result would still hold without the application of the filter. However, it would not be as clean as it appears from Fig. 16, partly because the observed variance in low-energy regions is primarily effected by the short-scale noise and normalized spectra $\hat{\Gamma}$ would then appear blurred at the long-wavelength part, which is of interest here.

In boundary current regions, baroclinic instability is believed to be the primary source of eddy kinetic energy. In an ideal geostrophically turbulent flow field (Kraichnan 1967; Charney 1971; Rhines 1979), the resulting kinetic energy should be close to $k^{-5/3}$ and k^{-3} relations at wavenumbers smaller and larger than the wavenumber of maximum instability, and should exhibit a maximum in eddy kinetic energy around a scale, usually referred to as the "β arrest" or "Rhines" scale, $L_{\mathrm{Rh}} = \sqrt{U/\beta}$ with U being a typical velocity scale and $\beta = \partial f/\partial y$, at which the "red" energy cascade comes to a halt as a result of Rossby wave dispersion. In terms of SSH spectra, this rule translates into $k^{-11/3}$ and k^{-5} power laws in $\Gamma_\zeta(k)$; but it is not clear to what extent isotropic and homogeneous geostrophic turbulence is fully developed in the oceans in the sense that regions are bounded and other dynamics might come into play (e.g., mode coupling through bathymetry).

If the turbulent energy cascade were localized in space, as is advocated for the oceans, then, as the energy evolves into a wavelike form, it should simply disperse by radiating Rossby waves. The nonlinear interaction of energy in the wavenumber domain then would largely cease, resulting in spectra of vastly different shape. Instead, the findings from this analysis can be summarized in a strikingly universal shape of wavenumber spectra over the entire extratropical World Ocean, suggesting that interior ocean dynamics are not significantly different from those near boundary currents. Note, that present velocity spectra are similar to previous finding from both the atmosphere and numerical ocean models (e.g., Julian et al. 1970; Frankignoul and Müller 1979; McWilliams and Chow 1981; Böning and Budich 1992).

4. Covariance functions and variability scales

There are various purposes, including the estimation of integral scales of variability or surface mapping, for which the covariance functions C, of ζ and δ are useful. Because the covariance function of a process is intimately related to its spectrum by the Fourier transform

$$C(t) = \int_{-\infty}^{\infty} \Gamma(\sigma) e^{i2\pi\sigma t}\, d\sigma, \tag{9}$$

the descriptions are mathematically equivalent, but complementary. In this section we will briefly describe covariance functions as they emerge from ζ and δ in space and time, after averaging over the same spatial extent as the corresponding frequency and wavenumber spectra discussed in the previous section. Similar to the close agreement of individual spectra, curves of individual estimates of C from 10° regions deviate only little from results shown.

a. Temporal covariances and timescales

The temporal correlation functions $C_\zeta(\tau)$ that correspond to the four averaged frequency spectra $\Gamma_\zeta(\sigma)$ given in Fig. 10a are displayed in Fig. 17a. Like those spectra, all autocorrelation functions are similar in their general shape. Variations in the first zero-crossing of individual curves are minor (between 70 and 80 days),

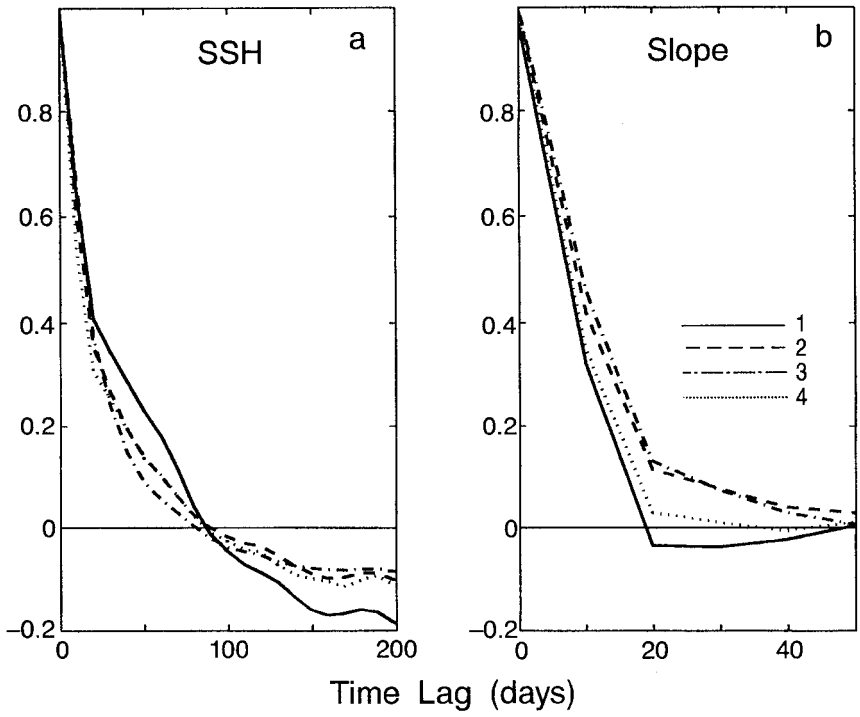

FIG. 17. Mean autocorrelation functions (a) $C_\xi(\tau)$ and (b) $C_\delta(\tau)$ averaged over the same regions as mean spectra in Fig. 7. Corresponding regions are marked in (b).

with the smallest values appearing in the high-energy regime. At small lags, the smallest correlations are associated with the area of minimum variability, that is, smallest signal-to-noise ratio (area 4). In terms of eddy velocity or surface slopes (Fig. 17b), their correlation drops rapidly below 0.5 everywhere within only a few repeat cycles. Both height and slope autocorrelation functions suggest an exponential decay with *e*-folding timescales of about 25–30 days for SSH and roughly 10–15 days for surface velocity measurements.

A measure of characteristic timescales of ocean variability is usually obtained from an integral over the small-lag positive fraction of the autocovariance function

$$T = C_\zeta^{-1}(0) \int_0^{T_0} C_\zeta(\tau)\, d\tau \qquad (10)$$

with T_0 being the first zero-crossing (e.g., Richman et al. 1977). A corresponding timescale T of SSH variability was computed from the autocovariance functions C_ζ in all individual 10° by 10° areas from the T/P data (Fig. 18). In the presence of significant negative lobes of the autocovariance functions it is more useful to compute the integral scale in its quadratic form

$$T_2 = C_\zeta^{-2}(0) \int_0^{T_{\max}} C_\zeta^2(\tau)\, d\tau, \qquad (11)$$

where $T_{\max}$ is the maximum time lag, usually taken to be one-half the length of the time series. Because this estimate appears more sensitive to small-lag noise effects, results are not shown, which generally agree with those from T.

In the Atlantic, the scales are qualitatively similar to previous Geosat results (Stammer 1992), but values are larger by about 30% because fluctuations at long periods (annual and interannual variability) were significantly removed from the Geosat analysis by the data processing scheme (orbit error correction). Overall, the emerging spatial pattern shows the largest timescales in the less energetic centers of the ocean, while energetic current systems are associated with shorter timescales. Interestingly, this finding does not apply to the Kuroshio.

Because of the presence of the strong seasonal and interannual (ENSO related) fluctuations in the T/P data, values in Fig. 18a are biased toward long scales. Removing all energy at annual and longer periods from the data prior to the computation of the integral timescale leads therefore to a noteworthy change in the amplitudes and geographical distribution of the resulting eddy timescale (Fig. 18b). Although the central subtropical gyres still show the longest scales, both boundary currents and the tropical ocean are now characterized by short-period variability. As a general result, eddy timescales vary by a factor of 5 between maxima in the subtropical gyres and high-latitude minima.

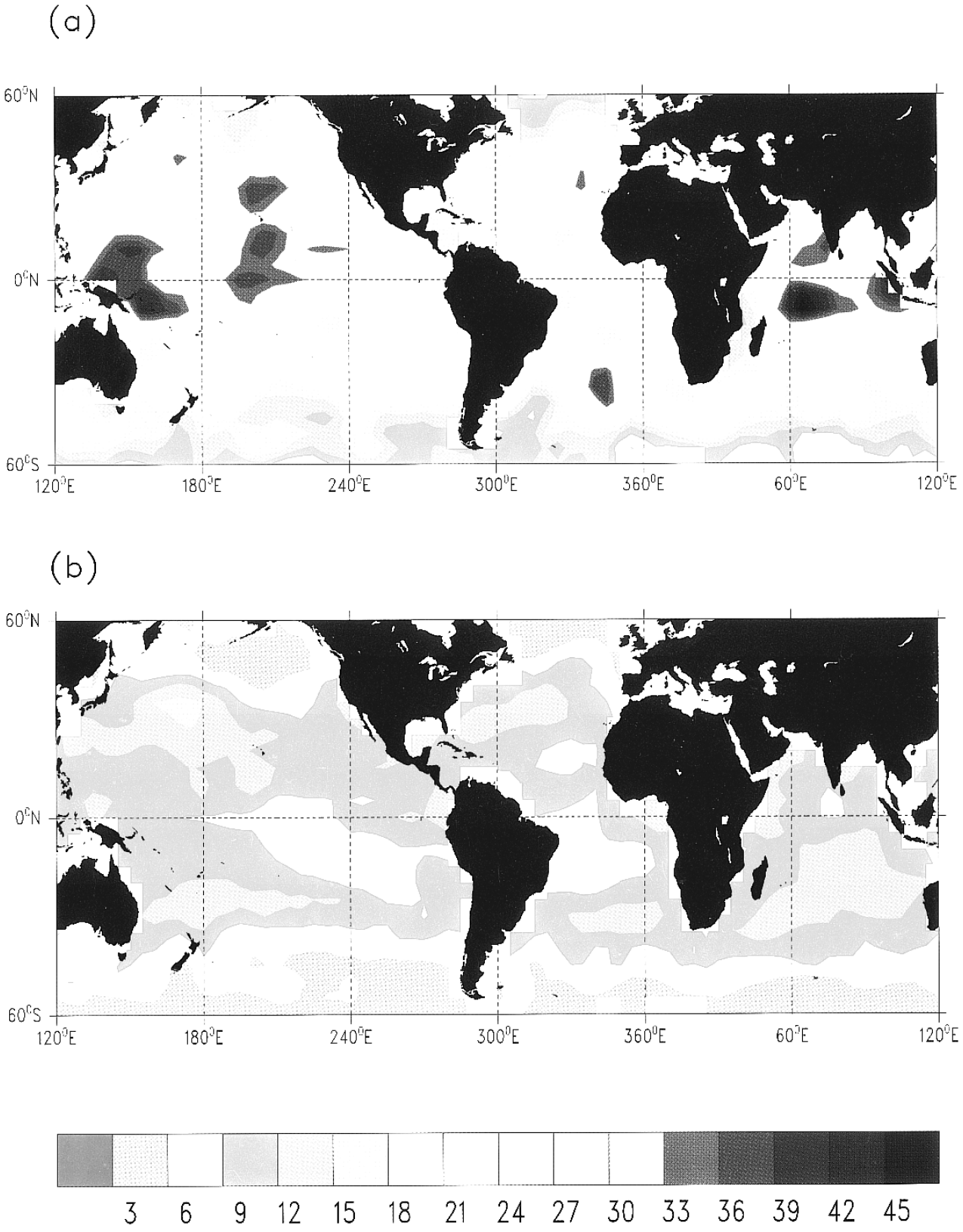

FIG. 18. Eddy timescales computed as an integral over the small-lag positive fraction of the autocovariance function $T = C_\zeta^{-1}(0) \int_0^{T_0} C_\zeta(s)\, d\tau$ with T_0 being the first zero-crossing. In (a) the full time series was used. In (b) the energy on annual and longer periods was removed prior to the scale estimation. Contour interval: 3 days.

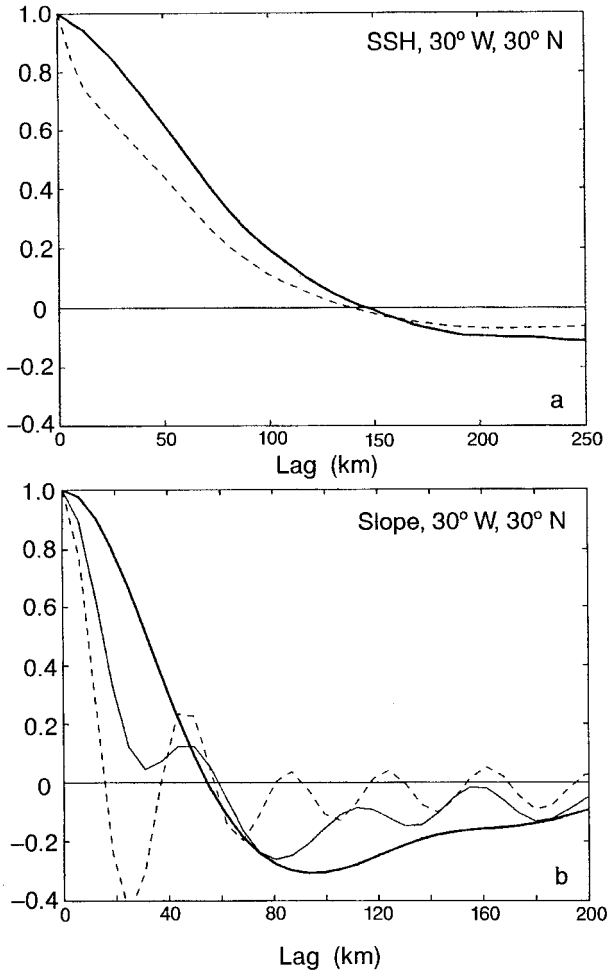

FIG. 19. (a) Mean spatial autocorrelation $C_\zeta(l)$ from the region 30°N, 30°W in the North Atlantic. The dashed line indicates initial results, and the solid line emerges after the optimal filtering. (b) Similar results but from $C_\delta(l)$. Dashed and thin solid line correspond again to the unfiltered and filtered results. The bold solid line emerges after the additional removal of all energy on wavelength smaller than 60 km by applying a nudge-filter.

b. Spatial covariances and scales

A pronounced drop in correlation is often found in alongtrack SSH autocorrelation functions over the first few lags from moderate or low energy areas of the oceans. This is demonstrated in Fig. 19a, which shows the $C_\zeta(l)$ curve representing the unfiltered alongtrack SSH data (dashed line) in the area centered at 30°N, 30°W in the Atlantic Ocean. It was argued previously that this initial drop is intimately related to noise in the altimeter observations (Stammer and Böning 1992). Based on (9) we have computed the autocorrelation functions as they result from the filtered spectra $\hat{\Gamma}_\zeta$ (bold line). It is clear that by removing the noise part of the spectrum most of the previous short lag distortion is eliminated, while leaving the zero-crossing basically unchanged.

The effect of filtering C_δ is demonstrated in Fig. 19b from the same area. Without any filter applied, the correlation drops to insignificant numbers after only a few spatial lags. After the optimal filter procedure, the correlation length has increased but still shows a distortion from the small-scale (white noise) energy visible in Fig. 16b. Upon an additional removal of all energy at wavelengths smaller than 60 km, the bold curve emerges.

Zonally averaged spatial correlation functions, $\langle C_\zeta \rangle$ and $\langle C_\delta \rangle$, are shown in Fig. 20 as a function of spatial lag as they result from the filtered spectra and are plotted separately from both hemispheres. The general tendency toward a more rapid drop and reduced scales of the zero-crossing toward high latitudes is apparent. Otherwise, the structure of the correlation functions is similar. The scale of the first zero crossing of $\langle C_\delta \rangle$ appears to be roughly one-half those from $\langle C_\zeta \rangle$ with negative lobes more pronounced.

Figure 21 shows the geographical distribution of the spatial eddy scales of SSH variability estimated from the lag of the first zero crossings of the spatial autocorrelation function $C_\zeta(l)$. Fields are shown with (Fig. 21a) and without (Fig. 21b) long-wavelength energy (a trend) in the data removed prior to the computation, respectively. Outside the Tropics, this operation has a visible impact primarily in the northeastern and southeastern Pacific, where a barotropic component was previously noticed in the wavenumber spectra.

A pronounced decrease in eddy scale with latitude is apparent in all oceans that is nearly symmetric to the equator. Optimally filtered spectra lead to integral-scale estimates that are consistent with (1/2) L_0, while unfiltered (noisy) data lead to systematically lower integral scales (see also discussion in SB96). These findings are highlighted in Fig. 22 showing zonal averages of spatial scales as they emerge from L_0, and from the integral length scale L of the raw and optimally filtered spectra in each individual $10° \times 10°$ boxes. [Plotted in the figures is $(1/2)L_0$ to facilitate a comparison.] In general, the change in eddy scale between low and high latitudes is about a factor of 2.5, globally, both from L_0 and the filtered L estimates [the somewhat different results by Hogg (1996) can be related to details in the analysis procedure].

5. Relation of eddy scales to L_{Ro} and L_{Rh}

Previous results suggest that physical processes leading to the observed mesoscale variability are surprisingly homogeneous geographically. Although direct wind forcing could be a significant eddy source term, its contribution to observed mesoscale variability seems to be limited to those locations where the general variability level is low and fluctuations in atmospheric forcing are high, notably the eastern North and South Pacific (Fu and Davidson 1995). Instead, results provided here strongly favor baroclinic instability as the dominant eddy source in the extratropical oceans. Supporting ev-

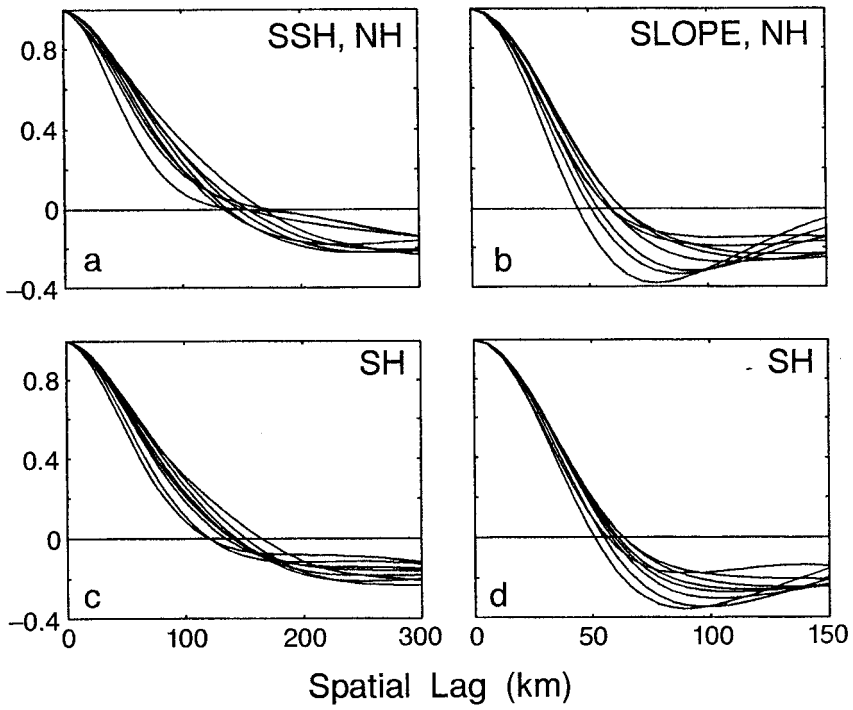

FIG. 20. Zonally averaged autocorrelation functions $\langle C_\zeta \rangle(l)$ (a,c) and (b) $\langle C_\delta \rangle(l)$ (b,d) from all latitudes, plotted as a function of spatial lag separately for both hemipheres.

idence for this hypothesis is obtained from the close relation between mean horizontal density gradients—equivalent to mean available potential energy—and from the spectral characteristics that are consistent with the theory of geostrophic turbulence. An analysis of ocean observations and numerical models in the North Atlantic led Beckmann et al. (1994) and SB96 to come to the same conclusion on a regional basis. Here we are able to show its truly global character.

Under uniform dynamical conditions, we should be able to find a close relation between eddy characteristics inferred from T/P data and mean flow properties. Such relations are advocated by theories describing amplitudes and transport properties of eddies in the presence of a baroclinically unstable flow field that were pioneered by Green (1970) and Stone (1972). Figures 3 and 4 indeed lend strong support to those theories in which baroclinic instability is the dynamical link between the ambient available potential energy of the mean flow field and observed eddy amplitudes.

A discussion of present results on eddy characteristics in the context of the theory of a baroclinically unstable flow field and an estimate of a related field of eddy diffusivity inferred from T/P data is provided in Stammer (1997). Here we restrict ourselves to a discussion of the relation of T/P eddy scales to those following from the first-mode baroclinic Rossby radius of deformation L_{Ro}, and the ''Rhines'' scale, L_{Rh}. The Rossby radius of deformation is of fundamental importance in atmosphere–ocean dynamics, both for the geostrophic equilibrium solution as well as transient ones. In the theory of baroclinic instability, it is closely related to the length scale of maximum eddy growth rates. In a strictly linear system both scales would be similar; however, in reality scales of the most unstable wave can be significantly larger (Simmons 1974).

A correlation of altimetric eddy length scales inferred from Geosat with the first-mode baroclinic Rossby radius was discussed previously by Stammer and Böning (1992) from a study in the Atlantic Ocean. A similar relation had been inferred before from local ensembles of eddies in selected (geographically limited) areas—for example, at the MODE and TOURBILLON sites (see Mercier and Colin de Verdiere 1985)—and from analysis of satellite sea surface temperature images and drifter data (Krauss et al. 1990).

For the present global comparison, we estimated L_{Ro} on a 1° grid over the global ocean from a local solution of the eigenvalue problem

$$\frac{\partial}{\partial z}\left[\left(\frac{f_0^2}{N^2}\right)\frac{\partial F}{\partial z}\right] + \lambda^2 F = 0, \tag{12}$$

subject to the boundary condition

$$\partial F/\partial z = 0 \text{ at } z = 0, -H.$$

Here N denotes the annual mean buoyancy frequency

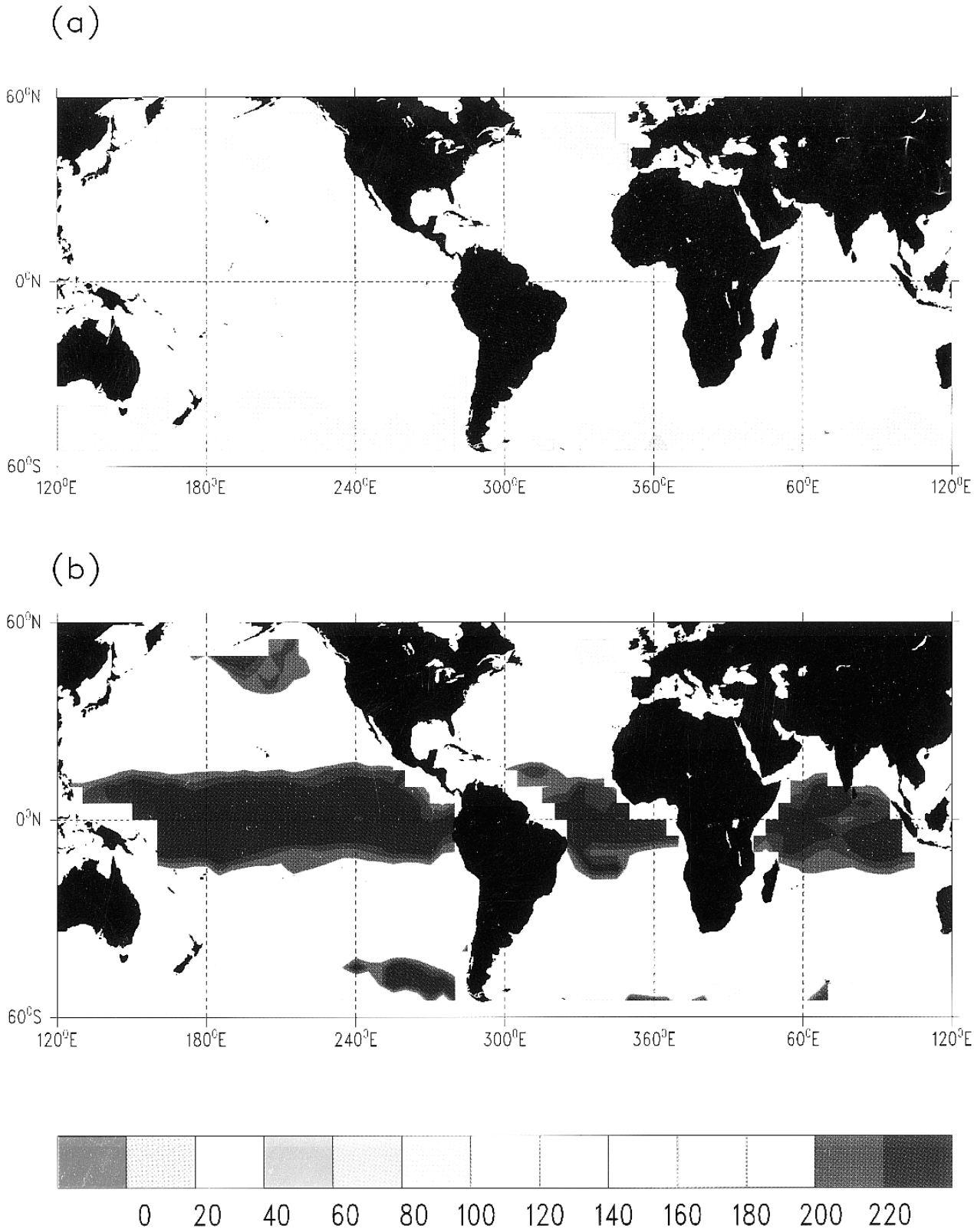

FIG. 21. Spatial eddy scale estimated from the first zero crossing of the spatial autocorrelation function $C_\varepsilon(l)$. In (a) a least squares slope was removed from the data prior to the computation, but not in (b). Contour interval is 20 km.

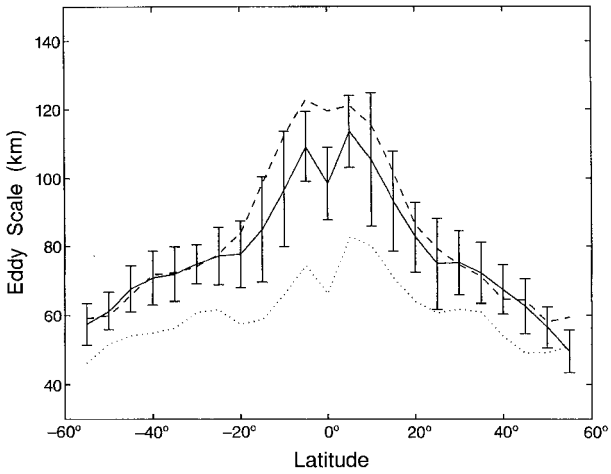

FIG. 22. (a) Eddy scales estimated from TOPEX data as the integral scale $L = C_\zeta^{-1}(0) \int_0^{l_0} C_\zeta(l)\, dl$ and the zero crossing L_0, and averaged zonally between 0° and 360° in longitude. Curves are the integral scale from filtered spectra (solid), the integral scale from raw data (dotted), and $(1/2)L_0$ (dashed).

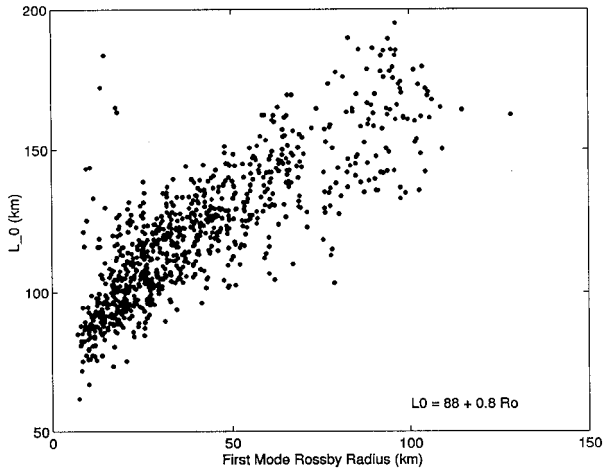

FIG. 24. Scatter diagram of L_0 from individual TOPEX areas against the corresponding Rossby radii of the first baroclinic mode for the global ocean. The correlation coefficient between both fields is $r = 0.81$.

computed from the Levitus et al. (1994) climatology. The resulting field $L_{\mathrm{Ro}} = \lambda_1^{-1/2}$ (Fig. 23c) is consistent with previous publications by Emery et al. (1984) and Houry et al. (1987), but shows substantially more fine-structure in the presence of a spatially variable topography $H(\lambda, \phi)$.

From T/P scales a linear relation with L_{Ro}, averaged on a 5° grid, follows on a global basis as (Fig. 24)

$$L_0 = 0.8L_{\mathrm{Ro}} + 88 \text{ km}, \tag{13}$$

with correlation $\tau = 0.81$. About the same relation is obtained from individual basins, which in the Atlantic Ocean reads $L_0 = 0.7\ L_{\mathrm{Ro}} + 88$ km. [Those relations are based on L_0 taken from Fig. 21a after elimination of a trend in the data. With the trend included in the analysis (Fig. 8b), the corresponding relation reads

$$L_0 = 1.3\ L_{\mathrm{Ro}} + 99 \text{ km } (r = 0.70),$$

consistent with an earlier finding from the North Atlantic given in SB96.]

We also find a linear relation between L_{Ro} and the scale of the first zero-crossing of the slope covariance C_δ. Poleward of 30° latitude it results in $L_{\delta 0} = 0.8L_{\mathrm{Ro}} + 43$ km. However, relevant for high latitudes, scales from C_δ are biased toward larger values because the applied extra filter step by which all energy at wavelength smaller than 60 km is completely removed from $\tilde{\Gamma}_\delta$ prior to the computation of C_δ (see above). On the other hand, there is still a considerable noise effect present in C_δ in low latitudes that leads to a decrease in $L_{\delta 0}$ equatorward of about 30° latitude. Because a factor of ~2 in scales between those from ζ and δ follows from Fig. 20, the results based on SSH should be closely related to those of sea surface slope (up to a scale factor).

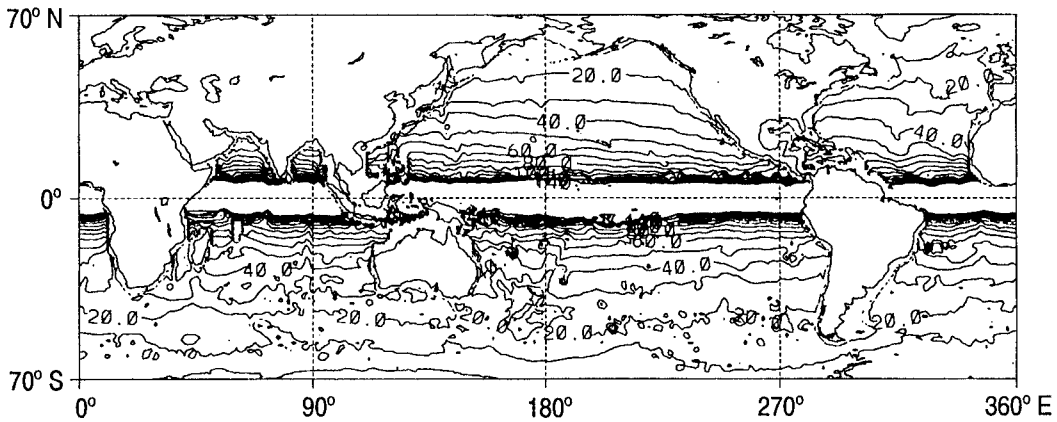

FIG. 23. First-mode Rossby radius of deformation as it follows from Levitus et al. (1994) hydrographic data as a solution of the Sturm–Liuville problem (see text).

A universal relation like (13), obtained from surface pressure data, suggests that first-mode processes dominate observed SSH fluctuations, globally. For a generalization of the result, a partitioning of SSH fluctuations into barotropic and baroclinic components would be necessary, which is not now generally available. An analysis of data from moored current meters, however, led Wunsch (1997) to the conclusion that the near-surface flow field in the interior ocean is primarily baroclinic and that barotropic contributions are becoming important only in the recirculation regime of boundary currents (high-latitude regions were not adequately sampled).

The high-resolution Community Modeling Effort of the North Atlantic, which also yielded a linear relation between eddy scales and L_{Ro} similar to (13), allowed more insight into the the effect of the barotropic energy on this relation (Beckmann et al. 1994). It was shown there that SSH spatial scales are increased as a result of a barotropic SSH component and that the purely baroclinic motion reflected in the sea surface variability indeed shows a direct proportionality with the deformation radius. Consequently, the offset between L_0 and L_{Ro} in Fig. 24 must be considered an artifact because of a barotropic (long wavelength) component in T/P observations.

A truly linear relation between L_ζ and L_{Ro} can be expected only from SSH signal associated with first-mode processes. It appears therefore straightforward to derive scale estimates directly from the cutoff wavenumber k_0 present in the wavenumber spectra Γ_ζ. In Fig. 25a, the associated spatial scale $L_c = (2\pi k_o)^{-1}$ is plotted (bold dots) as it results from the zonal-average wavenumber spectra given in Fig. 16. Indeed L_c shows a close relation to the zonal average L_{Ro} (open circles), to which it is similar in low latitudes. However, L_c is a factor of 3 larger in high latitudes (Fig. 25b).

For an interpretation of this peculiar result, it should be recalled that L_c is associated with the wavelength of maximum slope energy. Therefore, L_c either indicates the scale of instability, or, in the presence of geostrophic turbulence, it should be associated with $L_{\mathrm{Rh}} = \sqrt{U/\beta}$ at which (on a β plane) one expects the energy cascade from smaller to larger scales to be arrested (Rhines 1975). The occurrence of the related spectral peak at this transfer arrest wavenumber $(2\pi L_{\mathrm{Rh}})^{-1}$ has indeed been seen in a number of turbulence calculations (e.g., Haidvogel and Held 1980; McWilliams and Chow 1981; Held and Larichev 1996).

An estimate of a zonally averaged L_{Rh} scale is included in Fig. 25a, which follows from the assumption that $U = \sqrt{K_E}$, with K_E taken from Fig. 3a. Most noticeably, L_{Rh} is about 100 km poleward of 20° latitude and closely resembles both L_c and L_{Ro} in low latitudes. Moreover, the ratio L_{Rh}/L_c is nearly identical to L_c/L_{Ro}, while L_{Rh} is one order of magnitude larger than L_{Ro} in high latitudes.

The finding that L_c is much closer to L_{Ro} than to L_{Rh} over most of mid and high latitudes does suggest that a ''red'' energy cascade is not strongly developed there. Instead, the energy released by baroclinic instability from the mean-flow field appears to be kept near the input wavelength. This interpretation is consistent with the wavenumber spectra in Fig. 16b that reveal a $k^{-5/3}$ regime of a ''red'' energy cascade to be almost nonexistent in the high-latitude range. However, both Figs. 16 and 25 suggest the presence of a broader $k^{-5/3}$ regime toward low latitudes. McWilliams (1989) lists various physical mechanisms that could cause the inverse cascade to fail including too small a domain size, excessive Rossby wave influence, or a highly dissipative regime. [Because $L_{\mathrm{Rh}} \approx L_{\mathrm{Ro}}$ in the Tropics, higher-mode (smaller scale) processes are likely to dominate instability processes there (see also Wunsch 1997).]

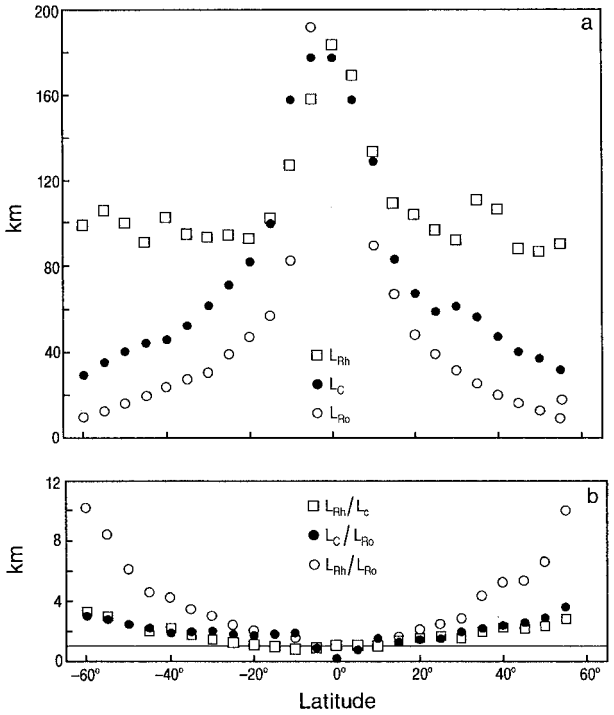

FIG. 25. (a) Zonally averaged first mode Rossby radius L_{Ro} computed from Fig. 18, (open circles) and spatial scale $L_c = (2\pi k_0)^{-1}$ (bold dots), where k_0 is the wavenumber of maximum kinetic energy in Fig. 13b. Open rectangles are estimates of a ''Rhines'' scale $L_{\mathrm{Rh}} = \sqrt{K_E^{1/2}\beta^{-1}}$, with K_E shown in Fig. 3a. (b) Ratios of L_c/L_{Ro} (bold dots), $L_{\mathrm{Rh}}L_{\mathrm{Ro}}$ (open dots), and L_{Rh}/L_c (open rectangles).

6. Global spectral relations

The similarity of wavenumber spectra from the global extratropical oceans discussed above suggests the existance of a universal description of wavenumber spectra of sea surface height and surface geostrophic velocity. In the following we will provide an estimate of such a relation. To do so we transform the alongtrack wavenumber k to a normalized wavenumber $\tilde{k} = k/k_0$, where

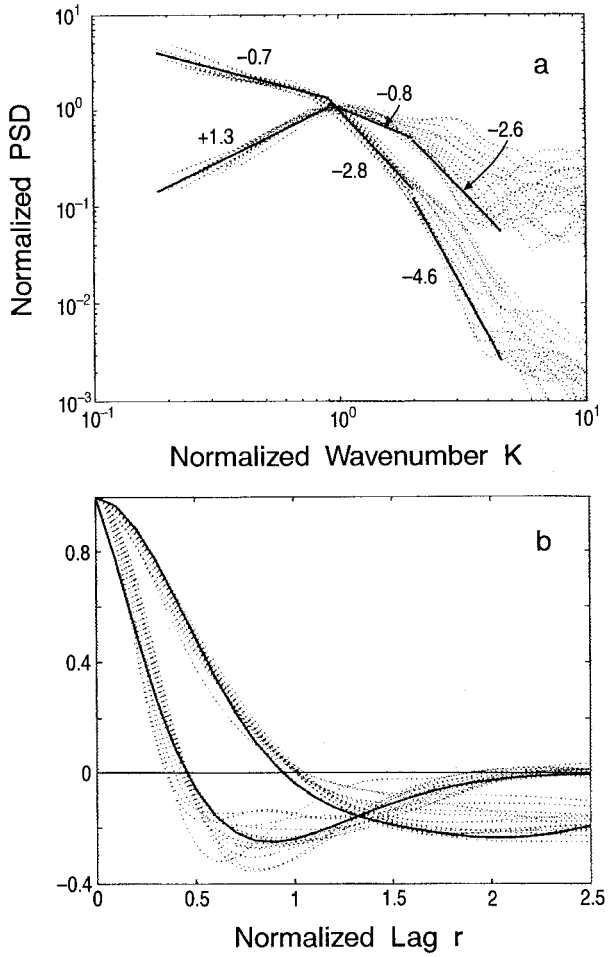

FIG. 26. (a) Zonally averaged wavenumber spectra $\langle\tilde{\Gamma}_\zeta\rangle(\tilde{k})$ and $\langle\tilde{\Gamma}_\delta\rangle(\tilde{k})$, $\tilde{k} = k/k_0$ and spectra are normalized by their respective energy at k_0. Bold lines indicate an analytic approximation (see text). (b) Zonally averaged autocorrelation functions $\langle C_\zeta\rangle(\tau)$ and $\langle C_\delta\rangle(\tau)$, where $\tau = l/L_0$. Bold lines indicate approximations in terms of polynomials (see text).

k_0 is the wavenumber of maximum energy in $\hat{\Gamma}_\delta$. This was done in Fig. 26a, showing $\langle\hat{\Gamma}_\zeta\rangle$ and $\langle\hat{\Gamma}_\delta\rangle$ curves as a function of $\tilde{k}$. In addition, individual curves were normalized by their energy at k_0 to accomplish an alignment also in the vertical. The results indicate a first-order description of wavenumber spectra in the general form

$$\Gamma_\zeta(k, \mathbf{x}) = \gamma_\zeta^2 \cdot \Gamma_0(\tilde{k}\cdot k_0) \tag{14}$$

$$\Gamma_\delta(k, \mathbf{x}) = \gamma_\delta^2 \cdot (2\pi k)^2 \cdot \Gamma_0(\tilde{k}\cdot k_0), \tag{15}$$

where γ_ζ^2 and γ_δ^2 denote the local variances of both fields, $\tilde{k}$ is a wavenumber, normalized by the local eddy scale $k_0 = (2\pi L_c)^{-1}$, and Γ_0 is a universal spectrum. Figure 4, in principle, allows one to relate observed eddy energy γ_δ^2 to the available potential energy embedded in the mean-flow field. From Fig. 25 a least squares solution for k_0 as a function of L_{Ro} and latitude ϕ reads

$$k_0\,(L_{\mathrm{Ro}}, \phi) = [2\pi(0.8 + \phi/25)\cdot L_{\mathrm{Ro}}]^{-1}. \tag{16}$$

From Fig. 26a an approximate analytic fit of Γ_0 follows as

$$\Gamma_0(\tilde{k}) = \begin{cases} 135\tilde{k}^{-0.7}, & 0.18 \le \tilde{k} \le 1.006 \\ 135\tilde{k}^{-2.8}, & 1.006 \le \tilde{k} \le 2.057 \\ 501\tilde{k}^{-4.6}, & 2.057 \le \tilde{k} \le 4.54. \end{cases} \tag{17}$$

Another approximation to the spectrum for the wavenumber range $0.18 \le \tilde{k} \le 4.54$, which is continuous in its first derivatives, is the Padé form (compare also WS95)

$$\Gamma_s(\tilde{k}) = \frac{-a_0 - a_1\tilde{k} + a_2\tilde{k}^2}{1 - b_1\tilde{k} + b_2\tilde{k}^2 - b_3\tilde{k}^3 - b_4\tilde{k}^4} \tag{18}$$

with coefficients $a_0 = 99.3$, $a_1 = 5.2 \times 10^2$, $a_2 = 1.5 \times 10^2$, and $b_1 = 9.8$, $b_2 = 13.6$, $b_3 = 7.6$, and $b_4 = 1.6$ (specific coefficients are sensitive both to the order chosen and the way in which the fitting was weighted, but the general shape appears stable). It is noteworthy that, while the steep decay of $k^{-4.6}$ is close to the theoretical k^{-5} relation, the intermediate regime is less steep than predicted by a $k^{-5/3}$ power law for velocity.

Similar to the spectrum, a universal analytic description of the correlation functions for ζ and δ can be specified in terms of a normalized spatial lag $r = l/L_0$, where L_0, as before, is the first zero-crossing of C_ζ; its relation to L_{Ro} follows from (13). An approximation of $C_\zeta(r)$ and $C_\delta(r)$ by higher-order polynomials leads to

$$C_\zeta(r) = e^{-0.61r^2}(1 - 2.72r^2 + 2.24r^3 - 0.51r^4 - 0.08r^5) \tag{19}$$

$$C_\delta(r) = e^{2.05r}(1 - 7.00r^2 + 5.13r^3 - 0.98r^4), \tag{20}$$

which are shown in Fig. 26b together with individual curves of $\langle C_\zeta\rangle(r)$ and $\langle C_\delta\rangle(r)$. The SSH covariance is related to those from the geostrophic alongstream and cross-stream velocity components as

$$R = -\frac{1}{r}\frac{dC_\zeta}{dr} \quad \text{and} \quad S = -\frac{d^2C_\zeta}{dr^2},$$

respectively (Bretherton et al. 1976; see also Freeland and Gould 1976). Assuming that S is describing the cross-track covariance, the corresponding relation holds only approximately here. As before, deviations are most likely due to the extra filter step involved in the computation of C_δ.

7. Concluding remarks

A major outcome from this study is that over most of the World Ocean, variability of sea surface height and surface velocity show strikingly universal characteristics. The largest variations in frequency and wavenumber spectra appear to be related to the geographically varying amplitude of eddy energy. This outcome appears to hold for both sea surface elevation ζ and surface geostrophic velocity or sea surface slope δ.

Frequency spectra can be described by three basic types representing (i) the tropical interior oceans, (ii) the bulk of the extratropical basins, and (iii) the energetic boundary currents. Apart from the tropical regime, spectra change to first order only in their local variance, and their shapes are always surprisingly close to the $\sigma^{-3/4}$ relation found in numerical simulations of geostrophic turbulence (McWilliams and Chow 1981).

Extratropical characteristics of wavenumber spectra were found to basically depend only on a poleward shift of its cutoff wavenumber, with spectral shapes otherwise being close to uniform. All sea surface height spectra show a plateau at long wavelengths and a pronounced cutoff followed by a steep spectral decay close to k^{-5} toward smaller wavelengths. In the low-latitude band, the energy distribution is ''red'' over a larger wavenumber range but leads also into a long-wavelength plateau when computed from lags spanning 20° latitudinally.

In terms of surface slope spectra, maximum energy is found at a wavenumber that corresponds to the cutoff wavenumber of SSH spectra. Energy decays toward smaller wavelengths in a manner consistent with the theory of baroclinic instability and geostrophic turbulence. This result is found basically over the entire extratropical ocean, where the variation of the eddy scale with latitude is significantly correlated with that of the first-mode Rossby deformation radius.

All those individual findings fit into the general hypothesis that baroclinic instability is the major eddy generation mechanism, not only near western boundary currents, but on a broad basis. Other eddy generation mechanisms such as direct atmospheric forcing are of some significance, but spatially limited to areas of low-level eddy energy with high atmospheric forcing. A barotropic, wind-induced, component in oceanic fluctuations should be enhanced in high latitude because of a decreasing vertical stratification and the associated increase in vertical penetration scale there (Philander 1978). This is consistent with findings from Fu and Davidson (1995), who report a significant correlation between changes in sea level and the wind stress curl only from the eastern North and South Pacific, and to some extent from the North Atlantic. It is those locations where we find the evidence of enhanced barotropic energy from this study (see Fig. 21b and Fig. 15).

There are various reasons to classify the present results as preliminary, including the existing uncertainties about the high wavenumbers in the data. But as time goes on, the T/P dataset will extend and improve in quality. In particular, more information will become available on T/P error characteristics. Another route to gain further confidence is to test numerical high-resolution ocean circulation models with respect to statistical relations and dynamical principles specified here from T/P data. Results will shed light on the validity of universal relations and allow more complete insight into dynamics than can be inferred from data alone.

It can be anticipated that the existence of universal eddy characteristics is of value for combining and understanding observations from diverse geographical locations. For that purpose, present results provided here only for near-surface conditions need to be extended into a full three-dimensional form. Ultimately analytic solutions are needed that combine eddy characteristics observed by altimetry and in situ data into one single theoretical framework.

Acknowledgments. I am indebted to Claus Böning, Lee-Lueng Fu, Jochem Marotzke, and Carl Wunsch for their helpful comments. This work was supported in part by Contract 958125 with the Jet Propulsion Laboratory and Grant NAGW-918 with the National Aeronautics and Space Administration.

REFERENCES

Beckmann, A., C. W. Böning, B. Brügge, and D. Stammer, 1994: On the generation and role of eddy variability in the central North Atlantic Ocean. *J. Geophys. Res.,* **99** (C10), 20 381–20 391.

Böning, C. W., and G. Budich, 1992: Eddy dynamics in a primitive equation model: Sensitivity to horizontal resolution and friction. *J. Phys. Oceanogr.,* **22,** 361–381.

Bretherton, F., R. Davis, and C. Fandry, 1976: A technique for objective analysis and design of oceanographic experiments applied to MODE-73. *Deep-Sea Res.,* **23,** 559–582.

Brügge, B., 1995: Near surface mean circulation and eddy kinetic energy in the central North Atlantic from drifter data. *J. Geophys. Res.,* **100,** 20 543–20 554.

Busalacchi, A. J., M. J. McPhaden, and J. Picaut, 1994: Variability in equatorial Pacific sea surface topography during the verification phase of the TOPEX/POSEIDON mission. *J. Geophys. Res.,* **99,** 24 725–24 738.

Chao, Y., and L.-L. Fu, 1995: A comparison between the TOPEX/POSEIDON data and a global ocean general circulation model during 1992–1993. *J. Geophys. Res.,* **100,** 24 965–24 976.

Charney, J. G., 1971: Geostrophic turbulence. *J. Atmos. Sci.,* **28,** 1087–1095.

Danztler, H. L., Jr., 1977: Potential energy maxima in the tropical and subtropical North Atlantic. *J. Phys. Oceanogr.,* **7,** 512–519.

Didden, N., and F. Schott, 1993: Eddies in the North Brazil Current retroflection region observed by GEOSAT altimetry. *J. Geophys. Res.,* **98,** 20 121–20 131.

Emery, W. J., W. G. Lee, and L. Maagard, 1984: Geographic and seasonal distribution of Brunt–Väisälä frequency and Rossby radii in the North Pacific and North Atlantic. *J. Phys. Oceanogr.,* **14,** 294–381.

Frankignoul, C., and P. Müller, 1979: Quasi-geostrophic response of an infinite beta-plane ocean to stochastic forcing by the atmosphere. *J. Phys. Oceanogr.,* **9,** 104–127.

Freeland, H. J., and J. Gould, 1976: Objective analysis of mesoscale ocean circulation feature. *Deep-Sea Res.,* **23,** 915–923.

Fu, L.-L., 1983: On the wave number spectrum of oceanic mesocale variability observed by the SEASAT altimeter. *J. Geophys. Res.,* **88,** 4331–4341.

——, and V. Zlotnicki 1989: Observing ocean mesoscale eddies from GEOSAT altimetry: Preliminary results. *Geophys. Res. Lett.,* **16,** 457–460.

——, and R. A. Davidson, 1995: A note on the barotropic response of sea level to time-dependent wind forcing. *J. Geophys. Res.,* **100,** 24 955–24 964.

——, E. J. Christensen, C. A. Yamarone, M. Lefebvre, Y. Ménard,

M. Dorrer, and P. Escudier, 1994: TOPEX/POSEIDON mission overview. *J. Geophys. Res.,* **99,** 24 369–24 382.

Gill, A. E., and P. P. Niiler, 1973: The theory of the seasonal variability in the ocean. *Deep-Sea Res.,* **20,** 141–177.

Green, J. S. A., 1970: Transfer properties of the large-scale eddies and the general circulation of the atmosphere. *Quart. J. Roy. Meteor. Soc.,* **96,** 157–185.

Haidvogel, D. B., and I. M. Held, 1980: Homogeneous quasi-geostrophic turbulence driven by a uniform temperature gradient. *J. Atmos. Sci.,* **37,** 2644–2660.

Held, I. M., and V. D. Larichev, 1996: A scaling theory for horizontally homogeneous, baroclinically unstable flow on a β-plane. *J. Atmos. Sci.,* **53,** 946–952.

Hogg, N. G., 1988: Stochastic wave radiation by the Gulf Stream. *J. Phys. Oceanogr.,* **18,** 1687–1701.

——, 1996: Oceanographic data for parameter estimation. *Modern Approaches to Data Assimilation in Ocean Modeling,* P. Malanotte-Rizzoli, Ed., Elsevier, 57–76.

Houry, S., E. Dombrowsky, P. DeMey, and J.-F. Minster, 1987: Brunt–Väisälä frequency and Rossby radii in the South Atlantic. *J. Phys. Oceanogr.,* **17,** 1619–1626.

Julian, P., W. Washington, L. Hembree, and C. Ridley, 1970: On the spectral distribution of large-scale atmospheric kinetic energy. *J. Atmos. Sci.,* **27,** 376–387.

King, C., D. Stammer, and C. Wunsch, 1994: The CMPO/MIT TOPEX/POSEIDON altimetric data set. Center for Global Change Science, Massachusetts Institute of Technology, Rep. 30, 33 pp. plus color plates. [Available from Center for Global Change Science, Massachusetts Institute of Technology, Cambridge, MA 02139.]

Kraichnan, R. H., 1967: Inertial ranges in two-dimensional turbulence. *Phys. Fluids,* **10**(7), 1417–1423.

Krauss, W., and C. W. Böning, 1987: Lagrangian properties of eddy fields in the northern North Atlantic as deduced from satellite-tracked buoys. *J. Mar. Res.,* **45,** 259–291.

——, R. Döscher, A. Lehmann, and T. Viehoff, 1990: On eddy scales in the eastern and northern Atlantic Ocean as a function of latitude. *J. Geophys. Res.,* **95,** 18 049–18 056.

Lanczos, C., 1959: *Applied Analysis.* Prentice-Hall, 539 pp.

Le Traon, P. Y., 1991: Time scales of mesoscale variability and their relationship with space scales in the North Atlantic. *J. Mar. Res.,* **49,** 467–492.

——, 1993: Comments on ''Mesoscale variability in the Atlantic Ocean from Geosat altimetry and WOCE high-resolution numerical modeling.'' *J.Phys.Oceanogr.,* **23,** 2729–2732.

——, M. C. Rouquet, and C. Boissier, 1990: Spatial scales of mesoscale variability in the North Atlantic as deduced from Geosat data. *J. Geophys. Res.,* **95,** 20 267–20 285.

Levitus, S., R. Burgett, and T. Boyer, 1994: *World Ocean Atlas 1994.* Vol 3: *Salinity*; Vol. 4: *Temperature.* NOAA Atlas NESDIS 3 & 4, U.S. Dept. of Commerce.

Ma, X. C., C. K. Shum, R. J. Eanes, and B. D. Tapley, 1994: Determination of ocean tides from the first year of TOPEX/POSEIDON altimeter measurements. *J. Geophys. Res.,* **99,** 24 809–24 820.

McPhaden, M. J., 1996: Monthly period oscillations in equatorial countercurrent. *J. Geophys. Res.,* **101,** 6337–6359.

McWilliams, J. C., 1989: Statistical properties of decaying geostropic turbulence. *J. Fluid Mech.,* **198,** 199–230.

——, and H. H. S. Chow, 1981: Equilibrium geostrophic turbulence I: A reference solution in a β-plane channel. *J. Phys. Oceanogr.,* **11,** 921–949.

——, and Coauthors, 1983: The local dynamics of eddies in the western North Atlantic. *Eddies in Marine Science,* A. R. Robinson, Ed., Springer-Verlag, 609 pp.

Mercier, H., and A. Colin de Verdiere, 1985: Space and time scales of mesoscale motions in the Eastern North Atlantic. *J. Phys. Oceanogr.,* **15,** 171–183.

MODE Group, 1978: The Mid Ocean Dynamic Experiment. *Deep-Sea Res.,* **25,** 859–910.

Müller, P., and C. Frankignoul, 1981: Direct atmospheric forcing of geostrophic eddies. *J. Phys. Oceanogr.,* **11,** 287–308.

——, and G. Siedler, 1992: Multi-year current time series in the North Atlantic Ocean. *J. Mar. Res.,* **50,** 63–98.

Nerem, R. S. and Coauthors, 1994: Gravity model development for TOPEX/Poseidon: Joint gravity model 1 and 2. *J. Geophys. Res.,* **99,** 24 405–24 448.

Pattullo, J. G., W. H. Munk, R. Revelle, and E. Strong, 1955: The seasonal oscillation in the sea level. *J. Mar. Res.,* **14,** 88–155.

Pedlosky, J., 1977: On the radiation of mesoscale energy in the mid-ocean. *Deep-Sea Res.,* **24,** 591–600.

Pèrigaud, C., 1990: Sea level oscillations observed with GEOSAT along the two shear fronts of the Pacific North Equatorial Countercurrent. *J. Geophys. Res.,* **95,** 7239–7248.

Philander, S. G. H., 1978: Forced oceanic waves. *Rev. Geophys. Space Phys.,* **16,** 15–46.

——, 1990: *El Niño, La Niña, and the Southern Oscillation.* Academic Press, 239 pp.

Press, W. P., S. A. Teukolsky, W. T. Vetterling, and B. P. Flannery, 1992: *Numerical Recipes.* Cambridge University Press, 963 pp.

Radok, R., W. H. Munk, and J. Isaacs, 1967: A note on mid-ocean internal tides. *Deep-Sea Res.,* **14,** 121–124.

Rhines, P. B., 1975: Waves and turbulence on a β-plane. *J. Fluid Mech.,* **69,** 417–443.

——, 1979: Geostrophic turbulence. *Annu. Rev. Fluid Mech.,* **11,** 401–441.

Richardson, P. L., G. E. Hufford, R. Limeburner, and W. S. Brown, 1994: North Brazil Current retroflection eddies. *J. Geophys. Res.,* **99,** 5081–5093.

Richman, J. G., C. Wunsch, and N. G. Hogg, 1977: Space and time scales and mesoscale motion in the sea. *Rev. Geophys.,* **15,** 385–420.

Robinson, A. R., 1983: *Eddies in Marine Science.* Springer-Verlag, 609 pp.

Rodríguez, E., and J. M. Martin, 1994: Assessment of the TOPEX altimeter performance using waveform retracking. *J. Geophys. Res.,* **99,** 24 957–24 970.

Schäfer, H., and W. Krauss, 1995: Eddy statistics in the South Atlantic as derived from drifter drogued at 100m. *J. Mar. Res.,* **53,** 403–431.

Schmitz, W. J., Jr., and J. R. Luyten, 1991: Spectral time scales for mid-latitude eddies. *J. Mar. Res.,* **49,** 75–105.

Shum, C. K., R. A. Werner, D. T. Sandwell, B. H. Zhang, R. S. Nerem, and B. D. Tapley, 1990: Variations of global mesoscale eddy energy observed from GEOSAT. *J. Geophys. Res.,* **95,** 17 865–17 876.

——, P. L. Woodworth, O. B. Andersen, G. Egbert, O. Francis, C. King, S. Klosko, C. Le Provost, X. Li, J. Molines, M. Parke, R. Ray, M. Schlax, D. Stammer, C. Tierney, P. Vincent, and C. Wunsch 1997: Accuracy assessment of recent ocean tide models. *J. Geophys. Res.,* in press.

Simmons, A. J., 1974: The meridional scale of baroclinic waves. *J. Atmos. Sci.,* **31,** 1515–1525.

Stammer, D., 1992: On mesoscale variability in the Atlantic Ocean—Analysis and assimilation of GEOSAT data (in German). *Ber. Inst. Meereskd Kiel,* **224,** 210 pp.

——, 1997: Steric and wind-induced changes in large-scale sea surface topography observed by TOPEX/POSEIDON. *J. Geophys. Res.,* in press.

——, and C. Böning, 1992: Mesoscale variability in the Atlantic Ocean from Geosat altimetry and WOCE high-resolution numerical modeling. *J. Phys. Oceanogr.,* **22,** 732–752.

——, and ——, 1993: Reply. *J. Phys. Oceanogr.,* **23,** 2733–2735.

——, and C. Wunsch, 1994: Preliminary assessment of the accuracy and precision of TOPEX/POSEIDON altimeter data with respect to the large-scale ocean circulation. *J. Geophys. Res.,* **99,** 24 584–24 604.

——, and ——, 1996: Generation and distribution of mesoscale eddies in the North Atlantic Ocean. *Warm Water Sphere of the*

North Atlantic Ocean, W. Krauss, Ed., Gebrüder Bornträger, 159–194.

——, R. Tokmakian, A. Semtner, and C. Wunsch, 1996: How well does a 1/4° global circulation model simulate large-scale oceanic observations? *J. Geophys. Res.,* **101,** 25 779–25 812.

Stone, P., 1972: A simplified radiative–dynamical model for the static stability of rotating atmospheres. *J. Atmos. Sci.,* **29,** 405–418.

Talley, L. D., 1983: Radiating instabilities in thin baroclinic jets. *J. Phys. Oceanogr.,* **13,** 2161–2181.

Tapley, B. D., and Coauthors, 1994: The JGM-3 gravity model. *Ann. Geophys.,* **12** (Suppl. 1), p. C192.

——, and Coauthors, 1996: The JGM-3 gravity model. *J. Geophys. Res.,* **101** (B12), 28 029–28 049.

Trèguier, A. M., and B. L. Hua, 1988: Influence of bottom topography on stratified quasi-geostrophic turbulence in the ocean. *J. Astrophys. Fluid Dyn.,* **43,** 265–305.

Vazquez, J., V. Zlotnicki, and L.-L. Fu, 1990: Sea level variability in the Gulf Stream between Cape Hatteras and 50°W: A Geosat study. *J. Geophys. Res.,* **95,** 17 957–17 964.

Wunsch, C., 1972: Bermuda sea level in relation to tides, weather, and baroclinic fluctuations. *Rev. Geophys.,* **10,** 1–49.

——, 1981: Low-frequency variability in the sea. *Evolution of Physical Oceanography,* B. A. Warren, and C. Wunsch, Eds., The MIT Press.

——, 1991: Large-scale response of the ocean to atmospheric forcing at low frequencies. *J. Geophys. Res.,* **96,** 15 083–15 092.

——, 1997: The vertical partition of oceanic horizontal kinetic energy and the spectrum of global variability. *J. Phys. Oceanogr.,* **27,** 1770–1794.

——, and A. E. Gill, 1976: Observations of equatorially trapped waves in Pacific sea level variations. *Deep-Sea Res.,* **23,** 371–390.

——, and D. Stammer, 1995: The global frequency-wavenumber spectrum of oceanic variability estimated from TOPEX/POSEIDON altimeter measurements. *J. Geophys. Res.,* **100,** 24 895–24 910.

Wyrtki, K., L. Magaard, and J. Hager, 1976: Eddy energy in the oceans. *J. Geophys. Res.,* **81,** 2641–2646.